DESIGN AND OPTIMIZATION OF A MINIATURE ACTUATOR USING SHAPE MEMORY ALLOY (SMA) WIRES

by

Morteza Teymoori

B.S., Biomedical Engineering, University of Isfahan, 2015

Submitted to the Institute of Biomedical Engineering
in partial fulfillment of the requirements
for the degree of
Master of Science
in
Biomedical Engineering

Boğaziçi University
2019

DESIGN AND OPTIMIZATION OF A MINIATURE ACTUATOR USING SHAPE MEMORY ALLOY (SMA) WIRES

APPROVED BY:

Assoc. Prof. Dr. Özgür Kocatürk .....
(Thesis Advisor)

Prof. Dr. Can Yucesoy .....

Prof. Dr. Kürşat Kazmanlı .....

DATE OF APPROVAL: June 2019

ACKNOWLEDGMENTS

I would like to thank my thesis advisor Assoc. Prof. Dr. Özgür Kocatürk for his constant support and availability throughout the project. I am also thankful to Ahmet Turan Talaş who helped me through the work and provided the necessary training regarding working in clean room. Abdülsamet Şahin is kindly acknowledged for offering his endless help.

Finally, I wish to thank my parents, Habibe Jalili and Mohammad Reza Teymoori, whose supports have been there in any possible form unconditionally. This thesis is dedicated to my beloved mom, my dad, and my sister.

ACADEMIC ETHICS AND INTEGRITY STATEMENT

I, Morteza Teymoori, hereby certify that I am aware of the Academic Ethics and Integrity Policy issued by the Council of Higher Education (YÖK) and I fully acknowledge all the consequences due to its violation by plagiarism or any other way.

Name :

Signature:

Date:

ABSTRACT

DESIGN AND OPTIMIZATION OF A MINIATURE ACTUATOR USING SHAPE MEMORY ALLOY (SMA) WIRES

Microfluidic systems have proven to be very beneficial in many fields such as chemical and biomedical sciences. The reduced sample volume, among many other advantages attracts researcher's attention to this technology. Consequently the need for a precise fluid handling and flow control is greater than before. Although many micropump systems have been invented over the last decade, there is still a need for a small, fast, quiet, and robust pump design. Because various applications have their own specific pumping requirements, the search for application driven novel micropump designs still continues. Shape memory alloys have been gaining more attention recently, for their idiosyncrasies, namely shape memory effect and pseudoelasticity. The ability of the shape memory alloy to recover high deformations makes them appealing for various applications. Here we use both of its hallmark behaviors, shape memory effect and pseudoelasticity, to design a cost-effective and versatile electrically driven actuator. To do so, we introduce a novel multistep 3D printing process for the batch fabrication of the device. For the characterization of the actuator, a conductive fluidic system was used and the obstruction level of a conductive fluid filled channel was quantified using impedance measurements of control fluid and used as an indicator of the actuation amplitude and rate. The fabricated actuator successfully closed the fluid channel even under fluid pressures of up to 150 mmHg with response time of under 100ms. This scalable design can be used in different applications such as micropump development, and microfluidic World to Chip interface.

Keywords: Shape Memory Alloys, Shape Memory Effect, Pseudoelasticity, Actuator, Micropump, Microfluidics.

ÖZET

ŞEKİL HAFIZALI ALAŞIM (ŞHA) TELLER İLE MİNYATÜR AKTÜATÖR TASARIMI VE OPTİMİZASYONU

Mikroakışkan sistemlerin kimya ve biyomedikal bilimler gibi birçok alanda faydalı olduğu kanıtlanmıştır. Diğer birçok avantajının yanı sıra indirgenmiş numune hacimleri araştırmacılarının ilgisini bu teknolojiye çekmektedir. Dolayısıyla, hassas sıvı dağıtımı ve akış kontrol teknolojilerine duyulan ihtiyaç eskiye nazaran daha fazladır. Son on yıl içerisinde birçok mikropompa icat edilmesine rağmen hala küçük, hızlı, sessiz ve sağlam pompa tasarımlarına gerek duyulmaktadır. Özellikle ısıya duyarlı biyolojik sıvıların iletimi ile ilgili uygulamalar için yeni mikropompa tasarım arayışı hala devam etmektedir. Şekil hafızalı alaşımlar psödo-elastisite ve şekil hafıza efekti olarak adlandırılan yapısal özellikleri sebebiyle çok dikkat çekmektedir. Şekil hafızalı alaşımların ileri seviye deformasyonlardaki hallerinden eski hallerine geri gelme yeteneği onları çeşitli uygulamalar için çekici hale getirmektedir. Bu çalışmada ekonomik ve farklı alanlarda kullanılabilen bir elektrikli aktüatör tasarlamak adına şekil hafızalı alaşımlara özgü psödoelastisite ve şekil hafıza efekti davranışlarının ikisi de kullanılmıştır. Aktüatörün çoklu üretimi için yeni bir çok aşamalı 3D yazıcı yöntemi sunulmuştur. Tasarımın iletken akışkan kanalını kapatma yetisi empedans ölçümleri ile irdelenmiş ve bu ölçümler aktüatörün hareket indikatörü olarak kullanılmıştır. İmal edilen aktüatör 150 mmHg'ya kadar olan basınçlarda bile başarılı bir şekilde 100 ms altında bir tepki süresinde ısıl izolasyon sağlanarak kanalı kapatmıştır. Bu ölçeklenebilir dizayn, mikropompa geliştirilmesi ve "World to Chip" arayüzü gibi çeşitli uygulamalarda kullanılabilir.

Anahtar Şözcükler: Şekil Hafizali Alaşim (ŞHA), nitinol, Işletici, Mikropompa, Mikroakişkanlar.

TABLE OF CONTENTS

LIST OF FIGURES

LIST OF TABLES

LIST OF SYMBOLS

MPa	Mega Pascal
MHz	Mega Hertz
μm	Micron
J/Kg	Joules per Kilograms
°C	Degree Centigrade
A_s	Austenite start temperature
A_f	Austenite finish temperature
M_s	Martensite start temperature
M_f	Martensite finish temperature
ε_t	Transformation strain
σ_s^A	Austenite start stress
σ_f^A	Austenite finish stress
σ_s^M	Martensite start stress
σ_f^M	Martensite finish stress
σ	Stress
ε	Strain
T	Temperature
GPa	Gigapascal
mg	Milligrams
° C/min	Degrees centigrade per minutes
%W/V	Weight per Volume concentration
V	Volts
$M\Omega$	Mega ohm
A	Amperes
ms	Milliseconds

LIST OF ABBREVIATIONS

SMA	Shape Memory Alloy
FEM	Finite Element Method
CAD	Computer Aided Design
SM	Shape Memory
SME	Shape Memory Effect
OWSME	One Way Shape Memory Effect
TWSME	Two Way Shape Memory Effect
MEMS	Microelectromechanical Systems
NiTi	Nitinol
UV	Ultra Violet
DSC	Differential Calorimetric Spectroscopy
MOSFET	Metal-Oxide-Semiconductor Field-Effect Transistor

1. INTRODUCTION

1.1 Microfluidics

Microfluidics is the science of manipulating fluids in small scales (10^{-8} to 10^{-9} liters). This is generally done through controlling the fluid flow in channels with microscale dimensions. These devices have gained significant attention over the recent years. Thanks to the physics in the microdimensions, such as dominance of laminar flow, higher surface to volume ratio, lower amount of working fluid, microfluidics opens a whole new alley of applications with higher accuracy, efficacy, and efficiency. For example, with ever growing need for more powerful processors and electronic chips, the demand for better cooling systems arises as well. Recently, the microfluidic liquid cooling systems have been explored more intensely because of their higher rate of heat transfer and appropriate sizes for the microelectronic industry [1, 2].

Microfluidic applications have gained more fame in the chemical and biological sciences than in any other field. The fluidic manipulation in microscale and its effects on the chemical and biological sciences has been compared to the invention of transistors and emergence of microelectronics. Many microfluidic chips have been designed for high throughput analysis of biomolecular signals, polymerase chain reaction, protein crystallization, mimicking the natural tissue (Organ on chips), and drug screening. Compared to the conventional methods for biological and chemical research, handling volumes of fluid in micro analysis systems (Microfluidic systems) offer much more advantages. Smaller systems mean smaller sample volumes, or reagents which can significantly drop the costs of research and diagnostics. The accuracy of the tests increases as the probability of molecular interactions increase in antigen-reagents interactions. These systems are generally made from disposable materials with closed channels which decreases the costs as well as the chance of contamination or the exposure of the operator to poisonous chemicals [2, 3].

Fluid manipulation in microscale is done via micropumps. Since the emergence of the microfluidics field, a wide range of micropumps have been invented. These are roughly categorized into two groups; Mechanical pumps which have a moving boundary or Electro-Magneto kinetic pumps where the direct conversion of energy occurs. While both categories have been divided into many subgroups, herein we are more interested in mechanical pumps with diaphragms that separate the working fluid from the displacement source (actuator). Figure 1.1 shows a schematic demonstration of a mechanical pump. In such devices with a pumping chamber and a diaphragm, pumping action is accomplished through controlling the fluid inlet, outlet, and the displacement of the diaphragm. Controlling of the inlet and outlet can be done through valves which allow the fluid to enter the pump chamber through the inlet when the diaphragm is contracted and leave the chamber through outlet when the diaphragm is expanded. These valves can be passive valves, such as the ones shown in the figure, or they can be active, where an energy source is necessary to actively open and close the channel synchronously. The schematic pump in Figure 1.1 pressurizes the fluid using a diaphragm which pushes out the fluid as it expands and refill the pumping chamber as it contracts. The energy for pressurizing the fluid in the pumping chamber can be obtained using various actuation mechanism such as Piezoelectric, Electrostatic, Thermal, Pneumatic etc. [3–5].

The applications of the microfluidic systems (e.g. point of care devices and portable electronics) imposes the necessity of reduction in the pump volume, weight, and sound noise as well. Thus, many on-chip micropumps have been developed, the most common type is the peristaltic micropumps which use the "Quake" valves in series to control the fluid flow. Figure 1.2 shows the schematic demonstration of a "Quake" valve and a peristaltic micropump designed using three valves in series. The valve consists of two channels that are aligned perpendicularly on two layers. The top and bottom channels consist of air and working fluid, respectively. Two channels are isolated with a thin membrane which can be deflected upon pressure increase in the air channel and obstruct flow of the working fluid. These valves are very small which makes them very appealing for achieving small footprint. However, the air control for the pneumatic actuation of these valves are done through a big Chip to World interface.

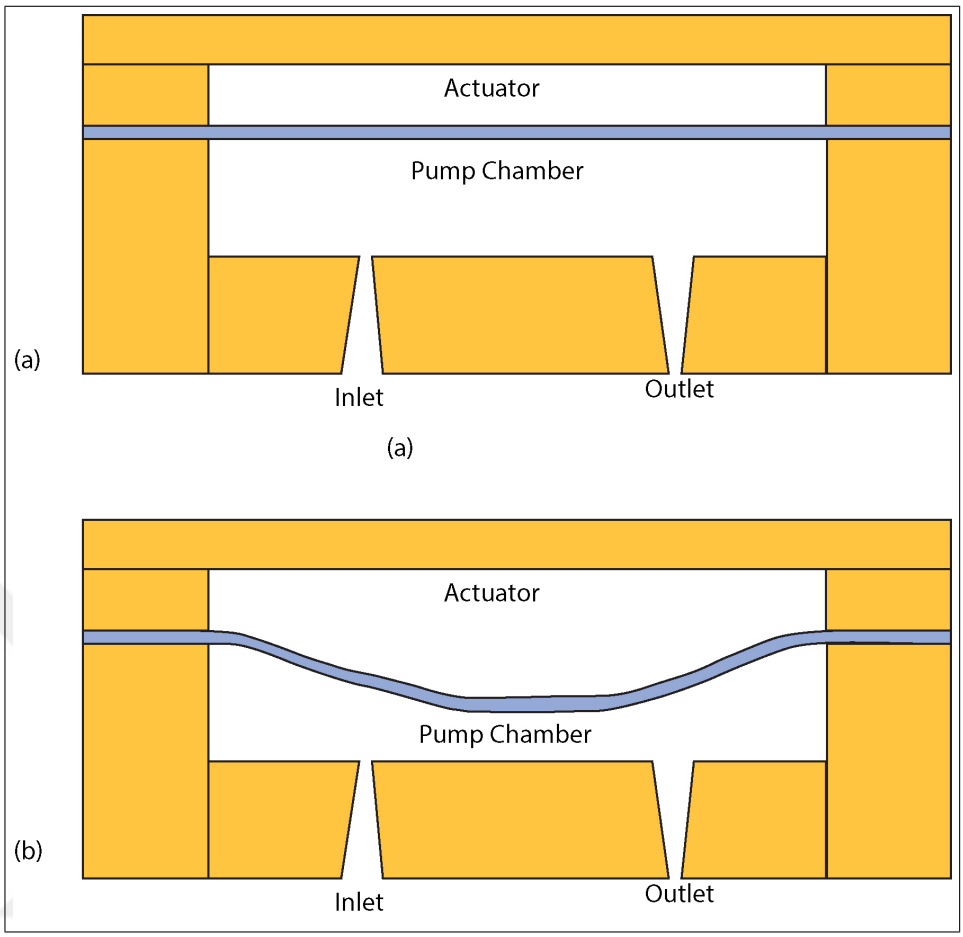

Figure 1.1 Illustration of a micropump with a diaphragm. Different actuation mechanisms can be used for the diaphragm displacement.

The air compressor and the control systems are bulky and hard to handle [6, 7]. Using other actuation mechanisms instead of pneumatics can omit such problems in newer pump designs.

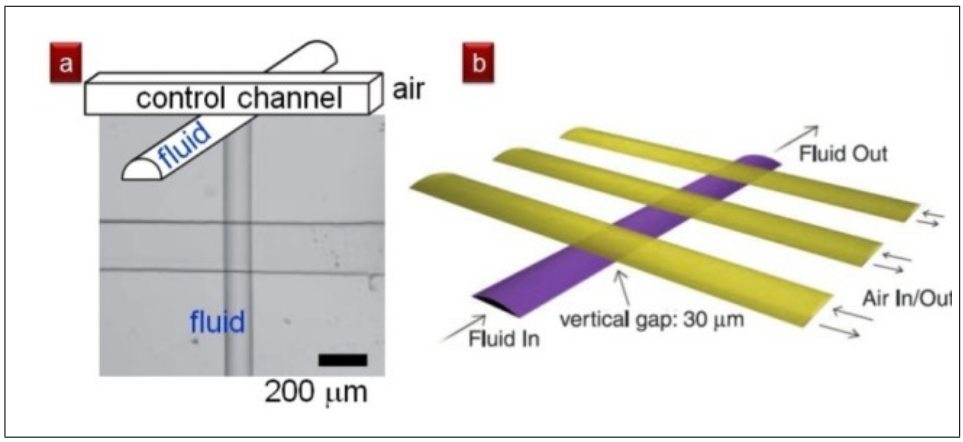

Figure 1.2 Pneumatic microvalve (a) and a peristaltic micropump (b) [6].

1.2 Active Materials and Actuators

With the advancement of technology, a need for materials with application specific properties has arisen. A group of materials with stronger mechanical properties that can exhibit additional engineering functionalities, known as multifunctional materials, has been emerged as the result of this demand. A special subgroup of these multifunctional materials, known as active materials, that show transducing and sensing capabilities have been discovered (e.g. Piezoelectric, Ionic electroactive polymers, Shape memory alloys, and shape memory polymers). The actuation behavior exhibited by these active materials are usually one or more orders of magnitude greater than that of the thermal expansion of the conventional materials, thus making them a significant part of the fields such as robotics and biomedical engineering [8].

The selection of an active material for a specific application can be done based on a set of parameters, the most important of which is the work density. Work density is defined as the product of stress and strain of the actuation or in other words, the amount of work done by the actuator in unit volume. This becomes more important in smaller scales, where the specific force requirements should be met in small dimensions. The actuation stress and range of actuation strain for different active materials are summarized in Figure 1.3. As it can be seen in Figure 1.3, while shape memory polymers exhibit the highest strain levels, they cannot provide high level of force.

Another important parameter when selecting the right actuation mechanism for an application is the actuator frequency. A simple comparison of the work density and the actuation frequency between different active materials is presented in Figure 1.4 [8].

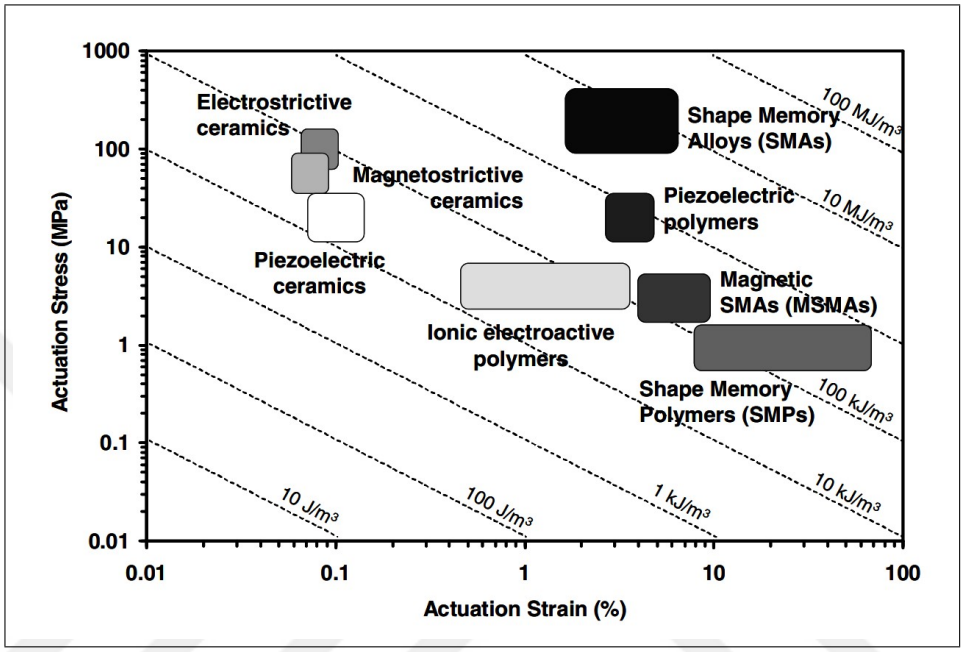

Figure 1.3 Actuation stress-strain of different active materials [8].

One of the most explored actuation mechanisms is piezoelectricity. Piezoelectricity is a phenomenon seen in some crystals, such as quartz. These crystals in certain electric field show a change in their structure by aligning the dipoles which is seen as a mechanical stress and shape change. Piezoelectric actuators can produce a relatively high force upon actuation (up to several MPa), however, thanks to the crystal structure of the material they have a very low limit of displacement which results in a small work density (Figure 1.4). The main advantage of these materials is the high actuation frequency which can reach up to 1 MHz. So far, the piezoelectric actuators have been mainly used for high frequency application where low stroke levels (less than 0.1%) would suffice [9]. However, the high achievable frequencies and stress production drove multiple investigators to remedy the problem of small stroke using various methods such as using piezoelectric bimorphs, or stacked piezoelectric discs [9]. Yun et al. [10] designed a bimorph piezoelectric actuator with the maximum actuation frequency of 15 Hz, but with a low force, 0.056N, and deformation of 63 μm deformation. Wood et

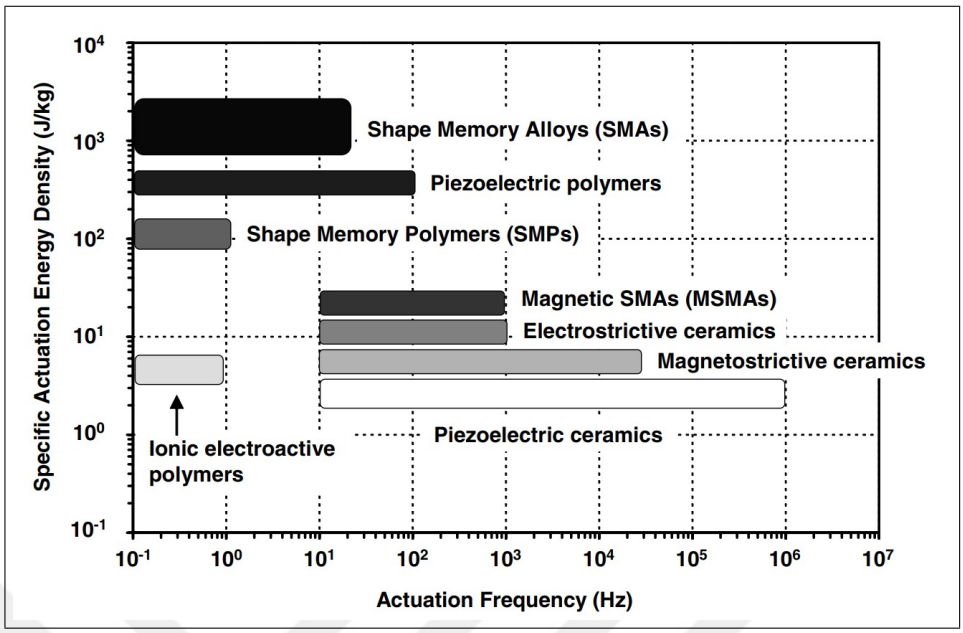

Figure 1.4 Actuation Frequency vs Work density [8].

al. [11] introduced another bimorph actuator that reached frequencies of up to 1 kHz and exhibited work density of 2 J/Kg with maximum stroke of 520 μm. The endeavor in development of the piezoelectric actuators culminated in deformations of up to 1.48 mm [12, 13]. Although these efforts were extremely successful in increasing the stroke, it is still not a significant stroke level for higher level fluid pumping applications [9, 14].

Due to the nature of the piezoelectric effect, these ceramics can operate in a split of a second with production of a high force with smaller strokes. Using a different physical concept, Ionic polymer-metal composites can produce higher stroke values while suffering from a low actuation frequency and force production. The mechanical nature of the ion transfer in the electric field is much slower than the dipole alignment in piezoelectric ceramics which results in slower actuation [9].

1.3 Shape Memory Alloys

Shape memory alloys are well known in robotics and biomedical devices due to their idiosyncratic behaviors. Superelasticity and shape memory effect, the two

prominent characteristics of these alloys, are the results of a martensitic and austenitic phase transformation between the soft martensite (lower Young's modulus) and stiffer austenite solid phases. These materials are capable of recovering a priorly set shape after extreme deformations (up to 8% strain). The programming is done through a heat treatment process at temperatures exceeding 400°C and is followed by rapid cooling (i.e. quenching in water) [8, 15].

Four important characteristic temperatures which are highly dependent on the SMA structure, composition, and heat treatment, are required while using SMAs. Austenite start (A_s), austenite finish (A_f), martensite start (M_s), and martensite finish (M_f) temperatures indicate the temperatures of the start and finish of the austenite and martensite transformations, respectively. These temperatures are stress dependent which is indicated in Figure 1.5. As the load on the material increases, the transformation temperatures increase as well [8].

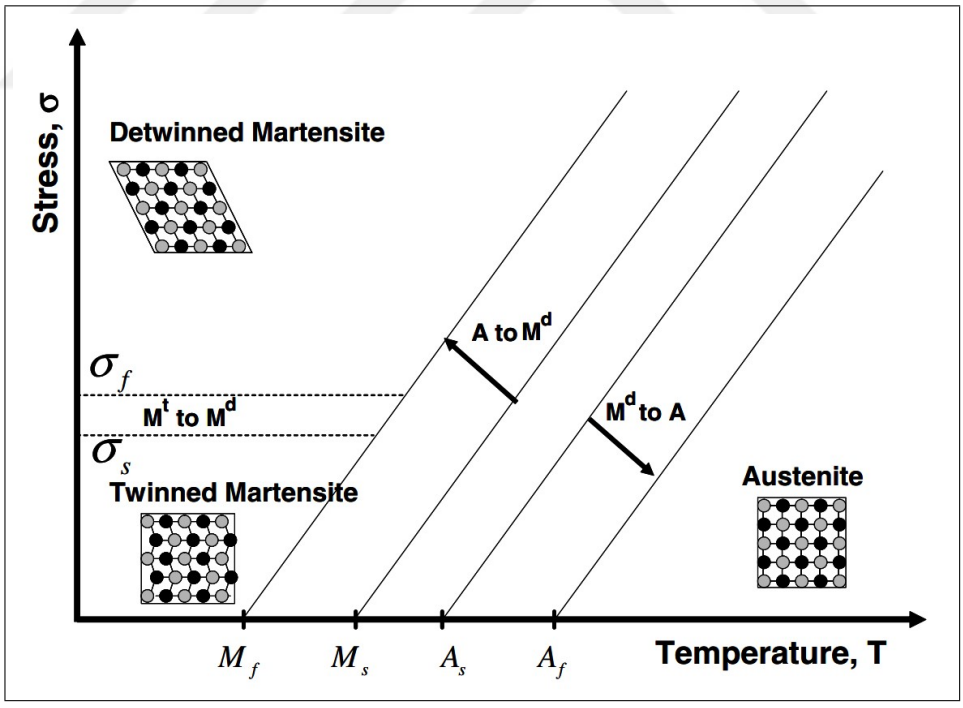

Figure 1.5 Phase diagram of a shape memory alloy. M^d to A and A to M^d indicate the reverse and forward transformations respectively [8].

Shape memory effect describes an SMAs behavior when it is deformed in its martensite phase and recover the parent phase upon heating above its A_f temperature.

Figure 1.6 shows the $\sigma - \varepsilon - T$ path of SME process. In its martensitic phase, an SMA without any applied load is in a twinned state which means that it consists of different martensitic variants. Once loaded, the material goes through an elastic deformation initially. As the stress levels reach to a certain threshold these martensitic variants start to align as one of them, the most energetically favorable one, starts to grow in expense of the others causing a macroscale deformation. This state of the material is called the martensite detwinned state. Once the transformation is completed, the material shows an elastic behavior once again. The observed strain at this level consists of an elastic and an inelastic part. This inelastic part of the deformation which is not recovered after removing the load is called the transformation strain (ε_t) and can be up to 8% based on the alloy's composition and other manufacturing parameters. Once the sample is heated at this deformed state, the material starts to go through a austenitic, or reverse, transformation which starts at A_s and completes at A_f temperature. During such transformation the SMA recovers its parent shape by removing the transformation strain (ε_t). It is worthy to note that if the sample is not load appropriately during cooling down to M_f, the forward transformation, material approaches its martensite twinned state without any significant shape change. These forward and reverse transformations are the main mechanisms which make SMAs appealing for the actuators' designs. As the SMA goes through the reverse transformation, it produces some work which can be utilized in engineering applications. The work produced in this process can be used in design of actuators. Figure 1.7 shows an actuator design using shape memory alloys for soft robotics [16].

Currently, most of the SMAs in use in the industry are pseudoelastic SMAs. Superelasticity, or more accurately Pseudoelasticity, denotes the stress-induced phase transformation of an SMA at temperatures higher than the alloy's A_f temperature. Usually pseudoelastic SMAs are tailored so that their A_f temperatures are below the temperature of their working environment, for instance, around 18°C so that they would go under a forward transformation upon loading in room temperature (25°C). Analogous to the temperature induced transformations, there are four important characteristic stress levels regarding the start and finish of the forward and reverse transformation, namely martensite start and finish stresses (σ_s^M, σ_f^M) and austenite start and

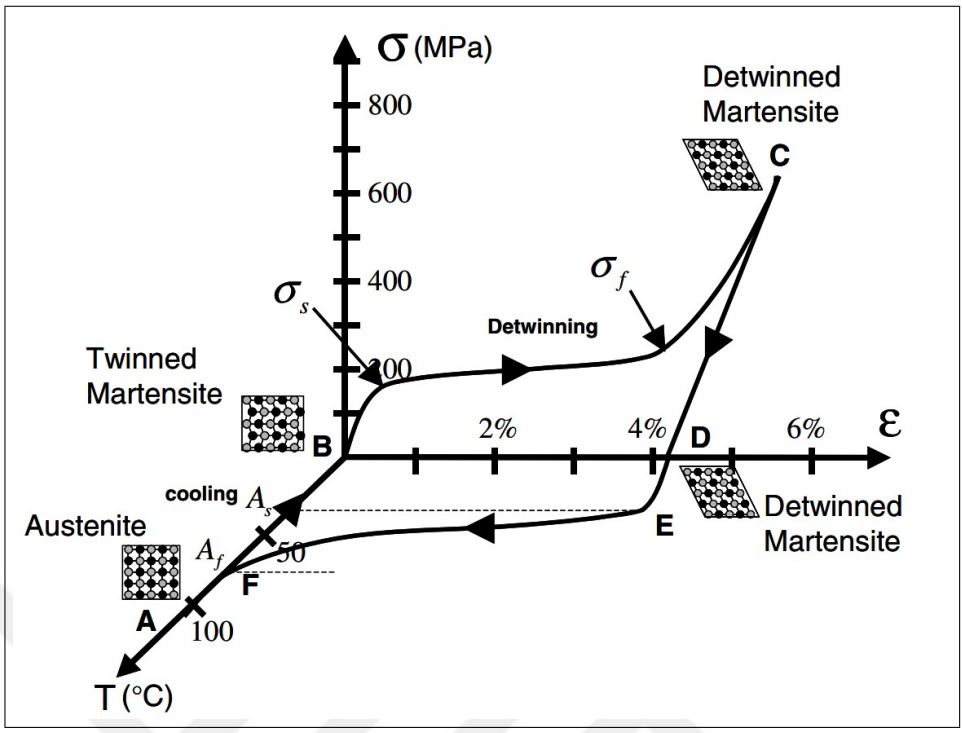

Figure 1.6 Shape memory effect's pathway in the stress-strain-temperature diagram [15].

finish stresses (σ_s^A, σ_f^A). As the temperature can be constant in this phase transformation, the $\sigma - \varepsilon - T$ diagram can be reduced to $\sigma - \varepsilon$ diagram in order to demonstrate pseudoelastic behavior. Figure 1.8 shows the $\sigma - \varepsilon$ path for a pseudoelastic SMA. As the material is loaded at temperatures above its A_f temperature, it initially displays the austenitic elastic behavior, however, once this stress exceeds the martensite start stress (σ_s^M) the material goes under a stress induced martensitic transformation (forward transformation) which is completed at (σ_f^M). The large inelastic deformation observed during this transformation is called the transformation strain that can rise to 10%. Once the transformation is completed the SMA starts to display martensitic elastic behavior again. Upon unloading, the material goes under a forward transformation starting at σ_s^A and finishing at σ_f^A. This recoverable strain makes these materials appealing for various industries such as medical field. A high number of stents, specially the stents for the peripheral vasculature where the deformations in the vessels are much more frequent due to the muscle movements, are made using the pseudoelastic SMAs [15, 17, 18].

Figure 1.7 A shape memory alloy based soft robot [16].

As it was mentioned before there are various methods of actuation, however, there is always a trade off between different aspects of an actuation mechanism. SMAs provide a high work density, low power consumption, simple control, and no sound noise. Moreover, they can work reliably for millions of cycles provided they are not loaded with high strains (lower than 5%) . However, the most important shortcoming of the SMAs is the recovery time. Since the recovery of the actuator is dependent on the cooling of the material, it is limited by the conductive and convective heat transfer. The mechanical nature of these methods reduces the frequency response of the actuator. However, it must be noted that many methods have been implemented to reduce this recovery time which can be applied to the actuator designs easily [19–23].

Shape memory behavior can be seen in two forms. The first and most common form is the one-way shape memory effect (OWSME) which denotes that the transformation from austenite to martensite upon cooling happens without any form of deformation. In other words, the SMAs martensite twinned state is similar to its austenite shape. The second form is the two-way shape memory effect (TWSME) that is exhibited in trained SMAs. A TWSM alloy has two stable shapes, one in the austenite form and one for the martensite form and it can cycle between these two forms upon heating and cooling. Although this behavior can seem appealing for many applications, there is a significant setback for these SMAs; they can perform smaller strain recovery upon cooling (2% compared to 6-8% upon heating) with much lower force production and thus failing the point of using SMAs in many cases [24].

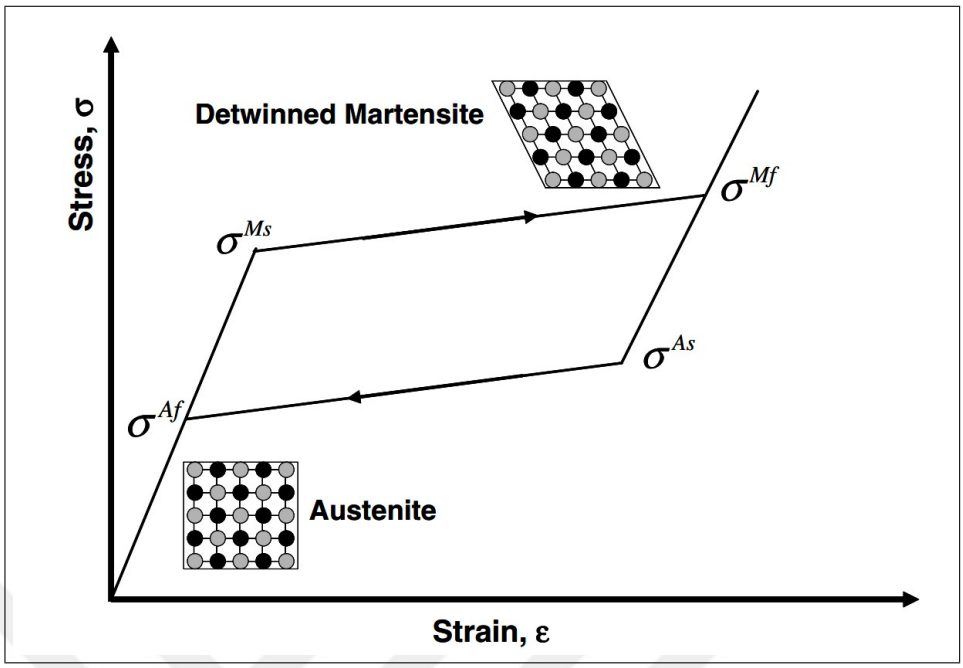

Figure 1.8 SMA Pseudoelasticity pathway.

Since there is no significant difference between the austenite and martensite twinned shapes in OWSME, there should be a bias force to deform the SMA at each cycle and transform the material from martensite twinned to detwinned state. Figure 1.9 shows a bimorph actuator design. In this type of actuators, at least two layers are used. One layer consists of the SMA which contracts when heated. The second layer is an elastic layer, composed of other materials such as cupper, that after being deflected during the actuation, recovers the initials shape of the actuator when left for cooling. The bimorph design has been explored more extensively in the microelectromechanical systems (MEMS) technology as its implementation is easier at microscale and nanoscale [25]. However, the microfabrication of the nitinol is the harder part. Various researchers have been studying the NiTi microfabrication and various deposition techniques, however, the nitinol proved to be more problematic at the heat treatment stage which is required in the formation of the idiosyncrasies of the SMA. Because of the expensive and complicated process of NiTi deposition, wafer level integration of the nitinol films has been explored and implemented for micro-designs as well. Sandstrom et al. [26] used bulk nitinol for development of bimorph micro cantilevers (Figure 1.9).

Another form of wafer level integration for smaller designs and lower costs is the

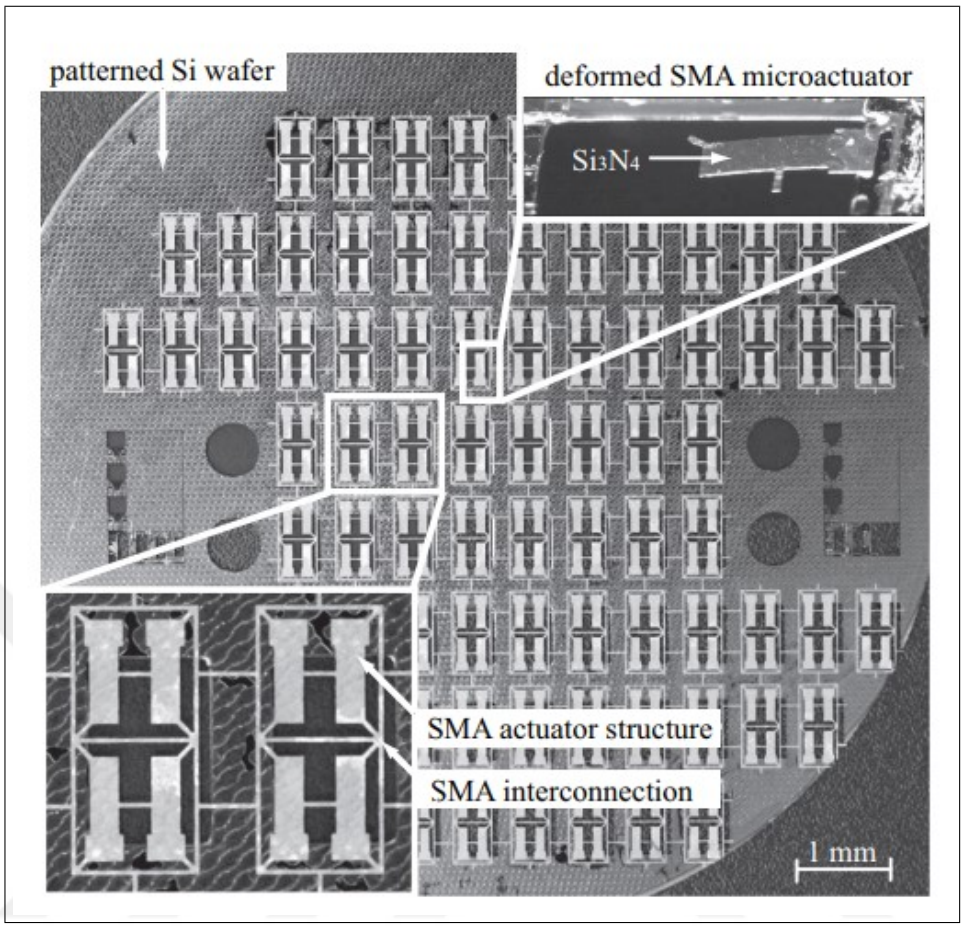

Figure 1.9 Bimorph cantilever (a), wafer integration of nitinol films (b) [26].

integration of nitinol wires. Nitinol wires are easy to use and commercially available with various diameters down to 25 μm at very low costs. Clausi et al [27–29] used a novel wafer integration method to develop micro cantilevers using commercially available nitinol wires with 37.5 μm diameter. Figure 1.10 shows the schematics of their cantilevers.

Although these wafer level integrations looked promising, these designs experienced serious bottlenecks regarding the wire fixation. Clausi et al [29] used SU8 as the fixing agent for the nitinol wires, however, it does not hold in high actuation temperatures after a couple of cycles. Additionally, the electrical connections at microscale proved to be problematic in such design. In order to solve these problems, same group used various methods such as wire bonding technology and nickel electroplating for higher mechanical stability and electrical conductivity [30, 31].

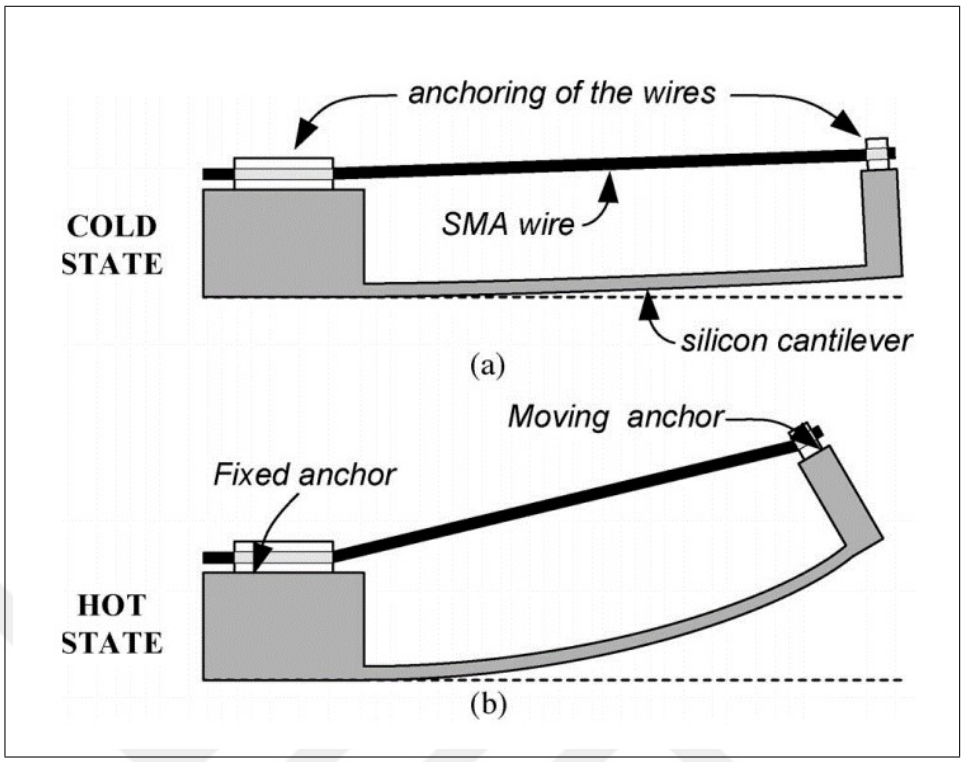

Figure 1.10 Wafer integration of the nitinol wires [27].

In this study we aim to use a similar principle to develop a novel actuation mechanism utilizing shape memory alloys. The objectives of this study can be summarized as following:

- Design and fabrication of a cost-effective actuator using commercially available shape memory alloys, on-board control units, and a 3D printing process.
- Complete isolation of the heat generating elements from the actuator element which poses serious problems in microfluidic applications.
- Development of a novel batch fabrication method for the integration of the wires SMA to the 3D printed frame using a multistep 3D printing processes.
- Demonstrate the applicability of such design as a mechanical actuator for diverse application with different response rate and actuation amplitude requirements.

2. MATERIALS and METHODS

2.1 Actuator Mechanism

Buckling is observed in beams when they are loaded axially but perform a sideways deformation. Usually engineers try to avoid this phenomena, however, in this design we benefit from the buckling behavior of a nitinol flat wire. The actuator design consists of a nitinol wire with shape memory and a pseudoelastic nitinol flat wire. Figure 2.1 shows the schematic of the design upon actuation. Two wires are coupled at the two ends of the actuator. One of the blocks at the two ends is fixed, while the other end is loose and can move freely between two planes. Initially, the active nitinol wire is heated through joule heating method. Upon exceeding its A_s temperature, the wire starts to shorten. Produced force is applied to the flat wire through the loose coupling block. The top cover of the actuator limits the system's displacement in perpendicular direction; subsequently, the flat wire, which is loaded axially, though asymmetrically, buckles once the force surpasses the critical beam load. This buckling profile can be used for various applications one of which is the squeezing and obstruction of a silicone tube.

Once the actuation signal stops, the pseudoelastic wire acts as a bias mechanism and recovers the deformation in the active nitinol wire. This way the active nitinol wire cycles between the detwinned martensite and austenite states.

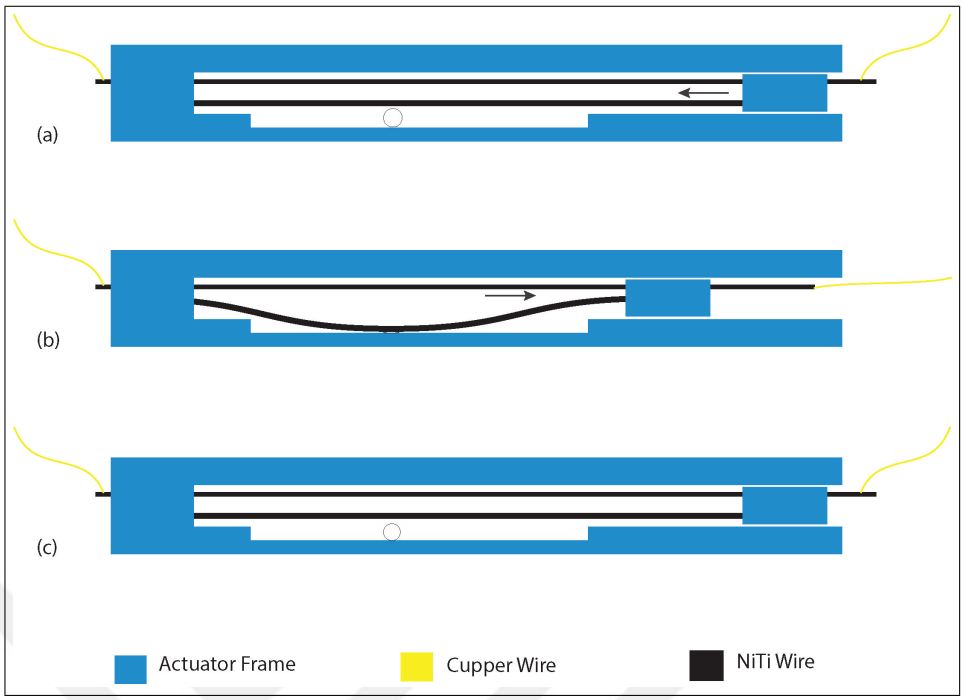

Figure 2.1 The schematic representation of the actuation mechanism. (a) the actuator at the beginning of the actuation cycle (the electrical signal begins). Once the wire is contacted and the flat wire goes through buckling (b), the signal is removed and the flat wire acts as a bias spring and recovers the inelastic deformation in the active nitinol wire (c).

2.2 Actuator Design Parameters

It is reported previously that in order to prevent any fatigue in cyclic loading of the SMA, the recoverable strain should be between 4% and 6% [23]. In order to predict the approximate dimensions of the design we used a finite element method. The buckling behavior of different lengths of SMA beam was modeled using COMSOL Multiphysics. The maximum sideways displacement of the beam with 5% nitinol recovery was taken as the stroke length. Since the load is applied completely symmetrical in the model, a temporary load was applied at beginning of the simulation perpendicularly to the middle of the beam in order to initialize the buckling profile. A gradual predefined displacement was applied from one end while the other end of the beam was fixed. The displacement was applied in 101 steps while the temporary perpendicular load was applied only in the first 30 steps. Elastic modulus and Poisson's ratio of 55GPa and 0.33 were used for the modeling of the beam [8]. Figure 2.2 shows the displacement contours of the beam with 20 mm length at the end of the loading.

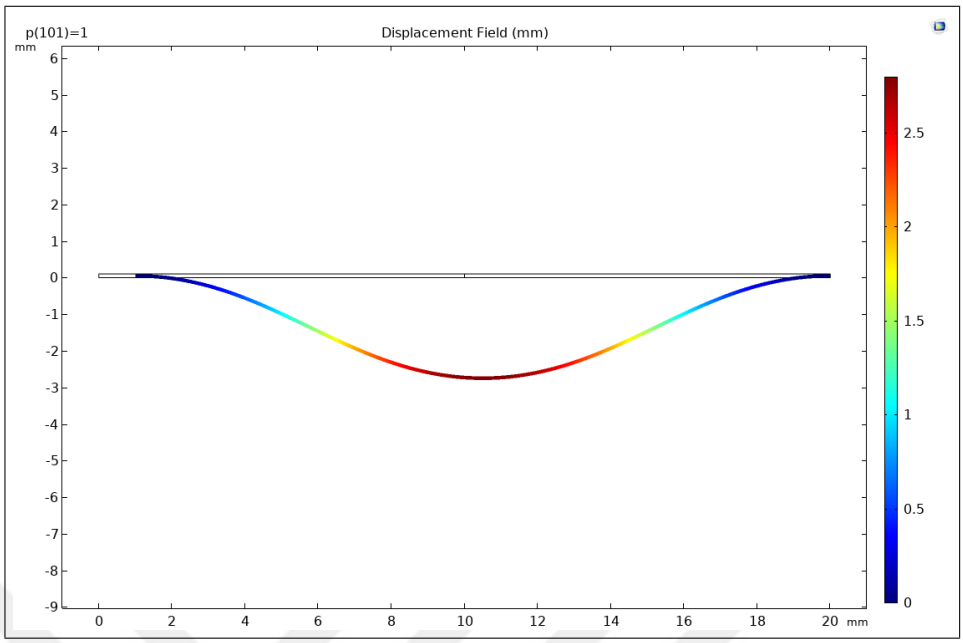

Figure 2.2 Displacement contours of a beam during buckling.

Beams with lengths between 5mm to 20mm were modelled and the maximum stroke length at the end of the actuation is plotted in Figure 2.3. As it is seen in Figure 2.3, the stroke length changes linearly with the length of the beam. This linear relation can be taken as a guide for choosing the actuator's dimensions. Since we produced the fluid channels with an outer diameter of 1mm, the length of the actuator was taken as 20 mm.

2.3 Batch Fabrication Method

A batch fabrication method has been developed for the fabrication of the actuator using 3D printing. A multi-step printing procedure has been utilized in order to integrate the pre-strained Flexinol wires with the printed frame. The actuator is comprised of a single printed part with the Flexinol wire and the nitinol wire embedded in the frame during the printing process. Thus, the printing consists of the multiple steps with interrupting the printer. The fabrication process is visualized schematically in Figure 2.4.

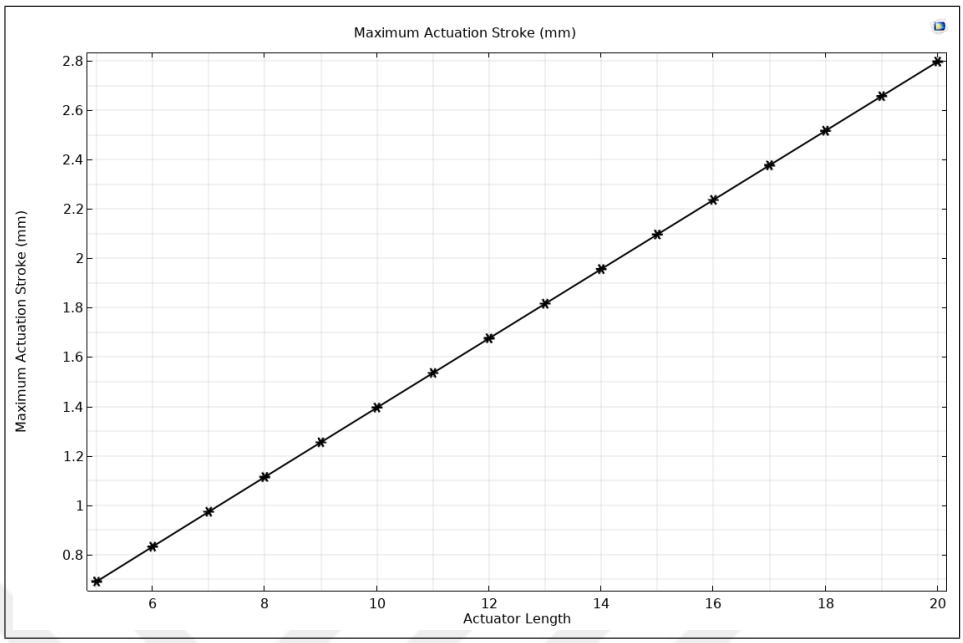

Figure 2.3 Stroke length of the beam with length between 5 to 20 mm.

The fabrication process can be briefly summarized in 6 steps.

1. The model is design using a Computer Aided Design (CAD) software (Solidworks). This model does not include the wires or any holes for the wires.

2. The 3D printer starts by printing a support layer, the thickness of which should be taken into account while calculating the first stop of the printer. Once the printing process has progresses up to the holding blocks at the two ends of the actuator, the printer is stopped.

3. Flat wires which were cut in length suited to the actuators' length are placed accordingly in the appropriate locations. The flat wires then are fixed at the both ends using UV-adhesives. As it is shown in Figure 2.5, the blocks at both ends are designed empty. This plays as a reservoir for the UV adhesive which has a much stronger bond with the wires compared to the 3D printing material.

4. The printing continues for 300-400 μm and then the process is interrupted once more.

5. Flexinol wire is then fixed at one end of the printing tray and stretched over the

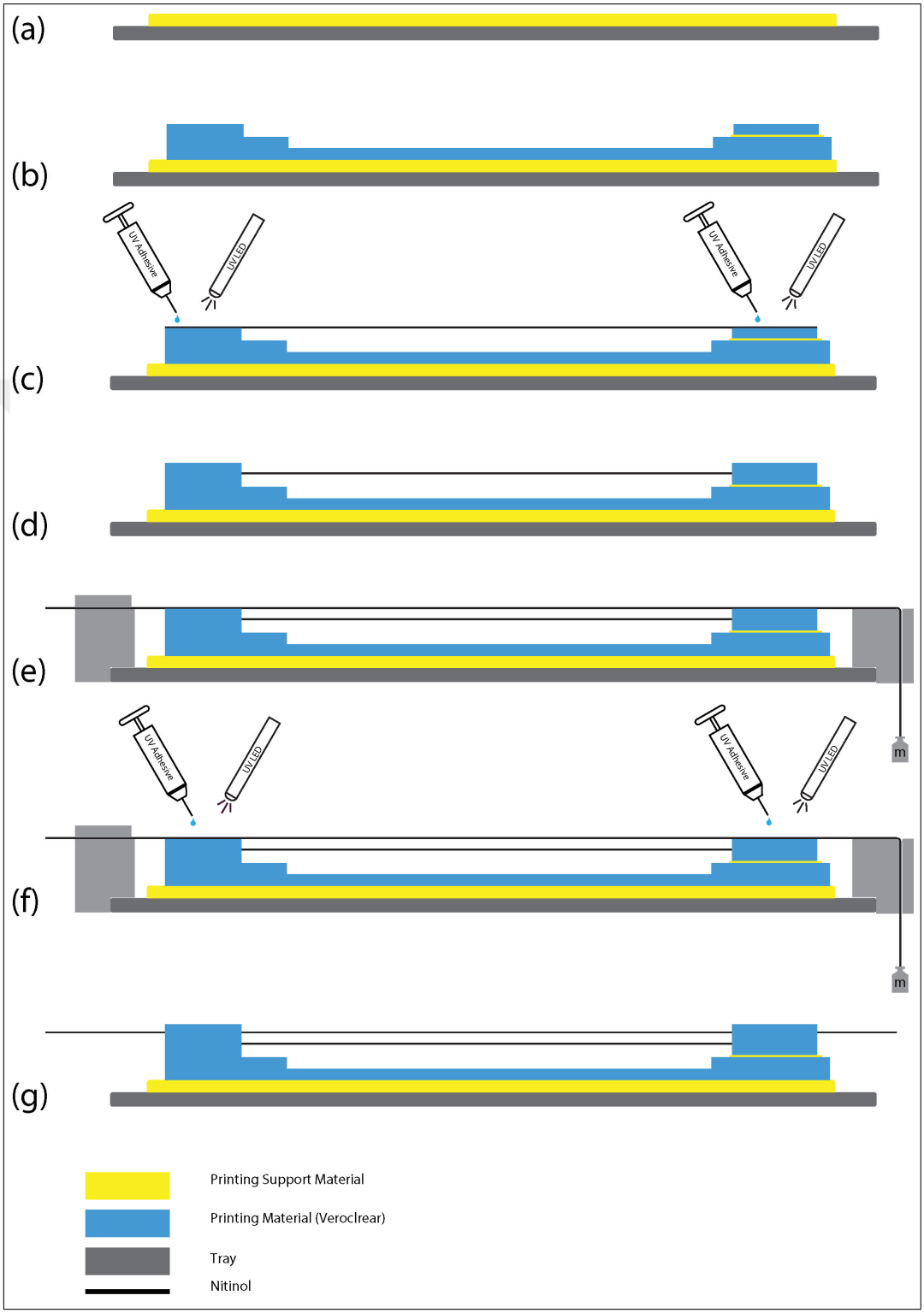

Figure 2.4 Batch fabrication process of the actuator.

actuators in a way that it passes over the blocks. At the other end of the tray, the wire is passed through a wire guide so it can be attached to a weight. This loading applies some load on the wire in order to pre-strain the wire. The amount of the weight is decided based on the wire diameter [23].

6. While the wires are under the constant stress, UV adhesive is used to fix the wire at the both ends of each actuator. Once finished, the load and the fixing apparatuses are removed, and the tray is relocated to the printer for the completion of the printing process.

It must be noted that the since the resolution of the printer is about 16 μm and the printing heads are very close to the printing surface, once the wires are places and fixed on the tray, the printing should be resumed at least 15 layers further than where it was stopped; thus, an additional height is considered in the designs for printing purposes.

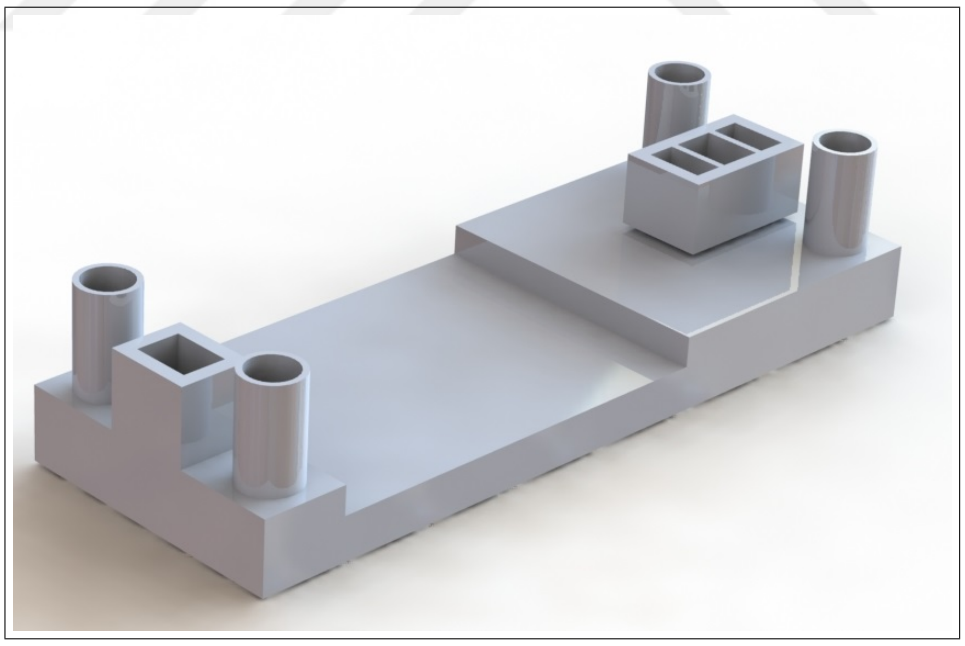

Figure 2.5 The actuator design in CAD software (Solidworks) prepared for printing.

2.4 Differential Calorimetric Spectroscopy

Differential scanning calorimetry (DSC) test was implemented using Perkin Elmer DSC 4000 device. Each sample weighted 2.85 mg. Test was carried out with a constant heating/cooling rate of 10°C/min from room temperature to 130° C. The process was preceded with a baseline measurement and removal of the thermal memory of the samples. The baseline measurement was carried out using the same test parameter without any nitinol samples inside. After sample placement the device was heated up to 130°C and kept at that temperature for 1 min and then cooled down to the room temperature using the same rate. After holding the sample in room temperature for 1 min, the DSC measurement began with the same parameters.

2.5 Nitinol Wires

Fort Wayne Inc. Pseudoelastic flat wires with 0.1mm × 0.5mm cross section were used as the buckling beams. Commercially available 0.1mm diameter nitinol wires were provided from Dynalloy Inc. Wires with 0.1mm diameter were used. Since nitinol needs to be deformed in the martensite state before it can be used as an actuator, a constant stress was applied during fabrication process in order to deform the wires before fixing them in place. We used a 57gr weight based on the data provided in the datasheet by Dynalloy for 0.1mm diameter wires [23].

2.6 Electrical Control Circuit

A circuit using Arduino Mega 2560 was designed for controlling the actuation and synchronized measurement of the sensors for current, and voltage measurements. LabVIEW program was used to control and acquire the data from the Arduino. Figure 2.6 shows the schematic of the control circuit. We used an IRL540n MOSFET for switching the voltage on and off for actuation. Arduino's digital pinouts can be used

in order to control the IRL540n.

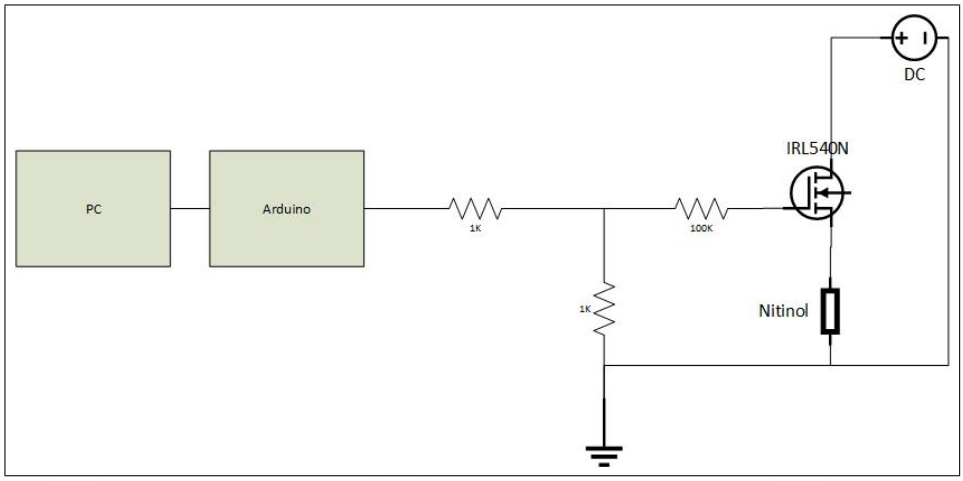

Figure 2.6 Schematic demonstration of actuator's control circuit.

For the actuator characterization purposes, an INA 260 digital sensor, provided by Texas Instruments, was used to measure the current and voltage applied to the actuator. Figure 2.7 shows INA260's circuit modification.

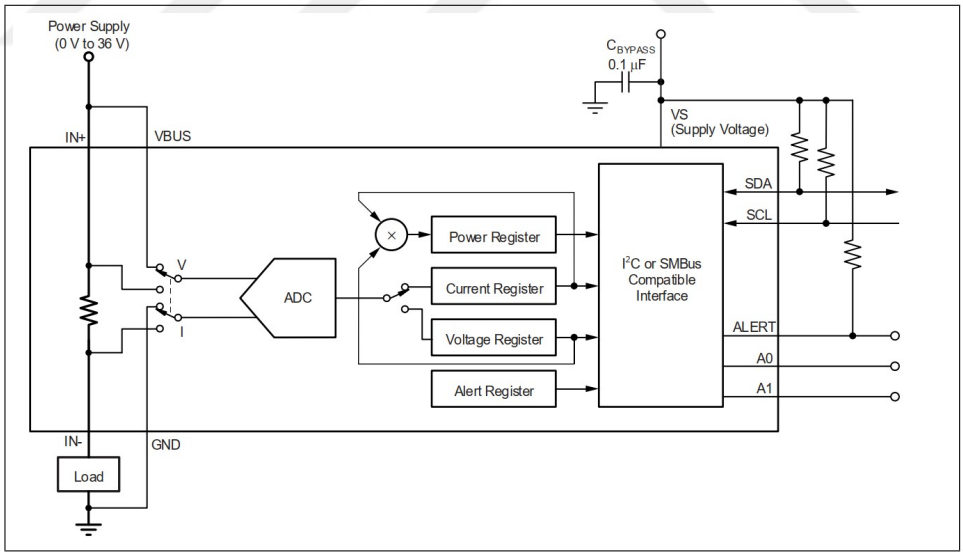

Figure 2.7 INA260 Circuit modification [32].

I2C protocol was used to communicate with the sensor. All the pins were connected according to the circuit modification suggested by the manufacturer (Figure 2.7). A0 and A1 pins were connected to the ground so the "1000000" binary address was used for the communication. The complete circuit diagram for the combination of the INA260 and the control circuit is shown in Figure 2.8 .

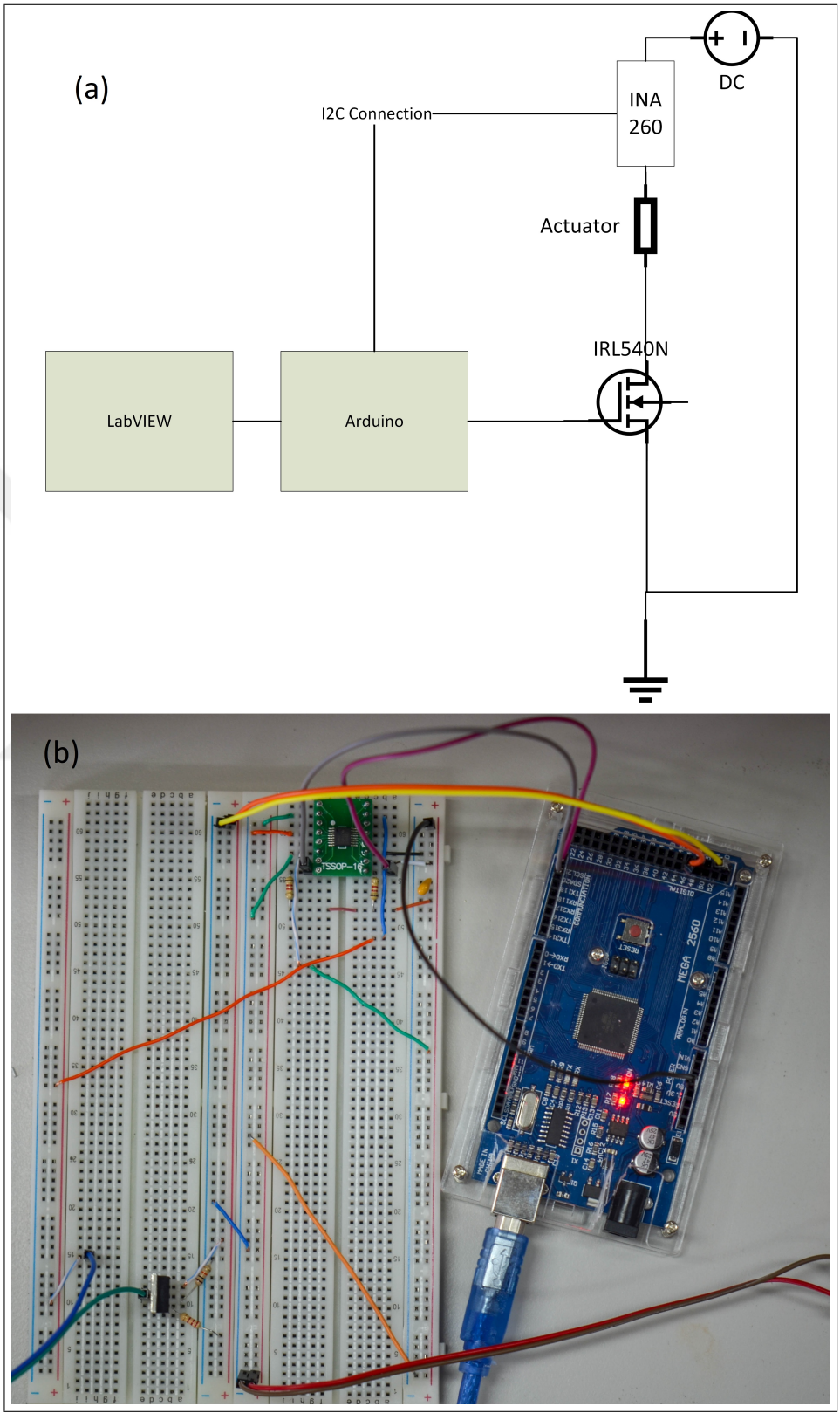

Figure 2.8 Control and measurement circuit. Schematic demonstration (a) and the circuit (b).

2.7 Actuation Response Time and Amplitude Measurement

In order to characterize the response rate and the actuation amplitude, a fluidic setup was created. A custom-made silicone tube (Ecoflex Silicone) with the inner diameter of 0.8mm and the outer diameter of 1mm was formed to be used as the fluidic channel in the actuator. The setup is shown in Figure 2.9. 10% W/V NaCl solution was used as the conductive working fluid. The impedance of the fluid in the channel is highly sensitive to the channel's cross section; thus, the changes in the channel impedance were taken as the indicator of the change in channel cross-section [33]. The impedance change rate was also interpretted as the actuation response rate. A Gwinstek LCR-8000G was used to measure the impedance of the fluidic channel. The measurements were done in room temperature at 100KHz and 2V AC. Impedance measurements were done at the maximum speed available which was limited to 120ms.

2.8 Actuator Fabrication

The actuators were fabricated using a 3D printer. Veroclear material was used as the printing material. Dymax 203A-CTH-F and 204-CTH was used in combination with a 1:1 ratio for fixing the wires in place.

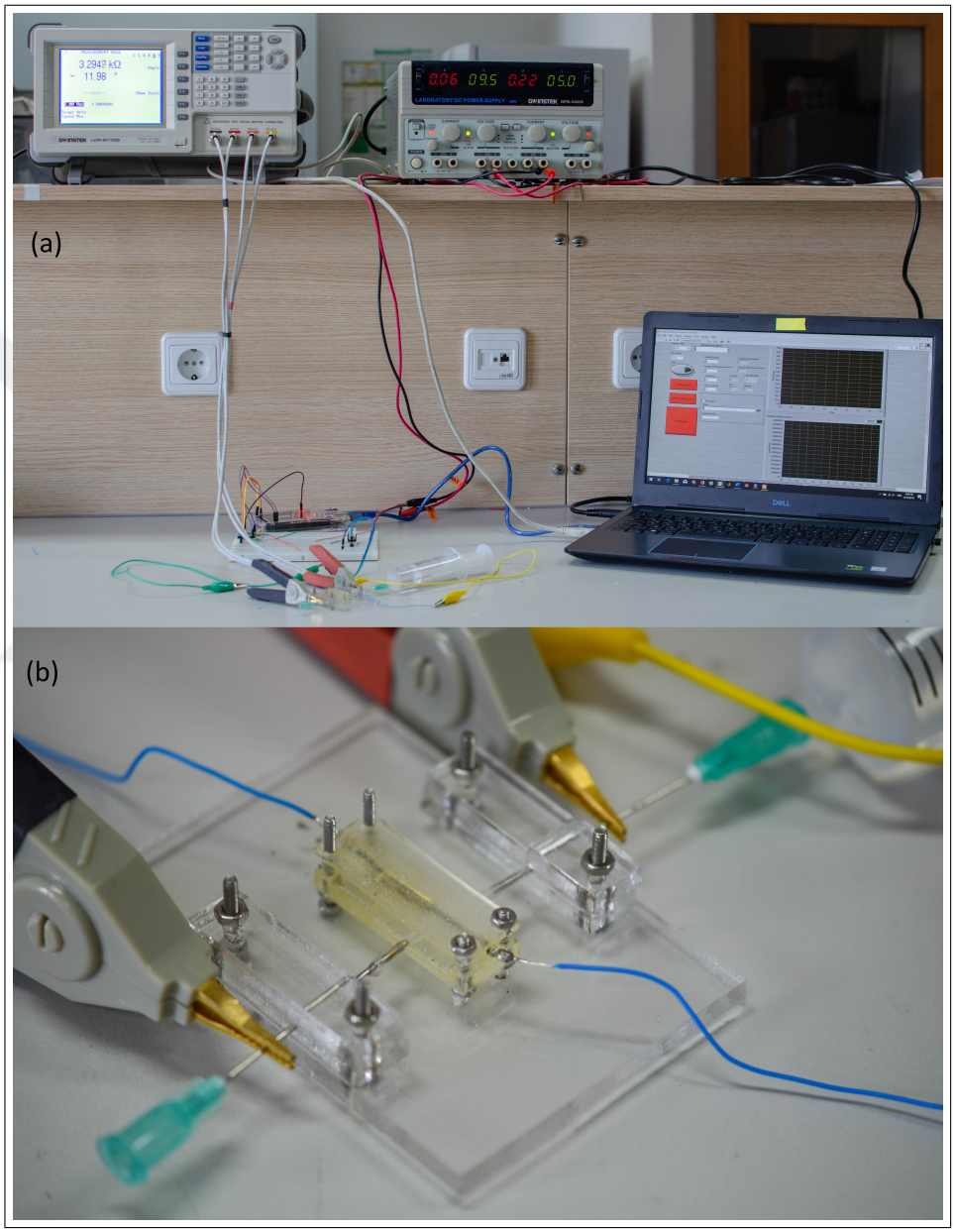

Figure 2.9 (a) Measurement setup, and (b) actuator test bench.

3. RESULTS

Figure 3.1 shows the DSC results in a heating and cooling cycle of a nitinol wire. A tangential line method is used to extrapolate the characteristic temperatures of martensitic and austenitic transformations, M_s, M_f, A_s, and A_f. Table 3.1 shows the acquired transformation temperature for flexinol wires.

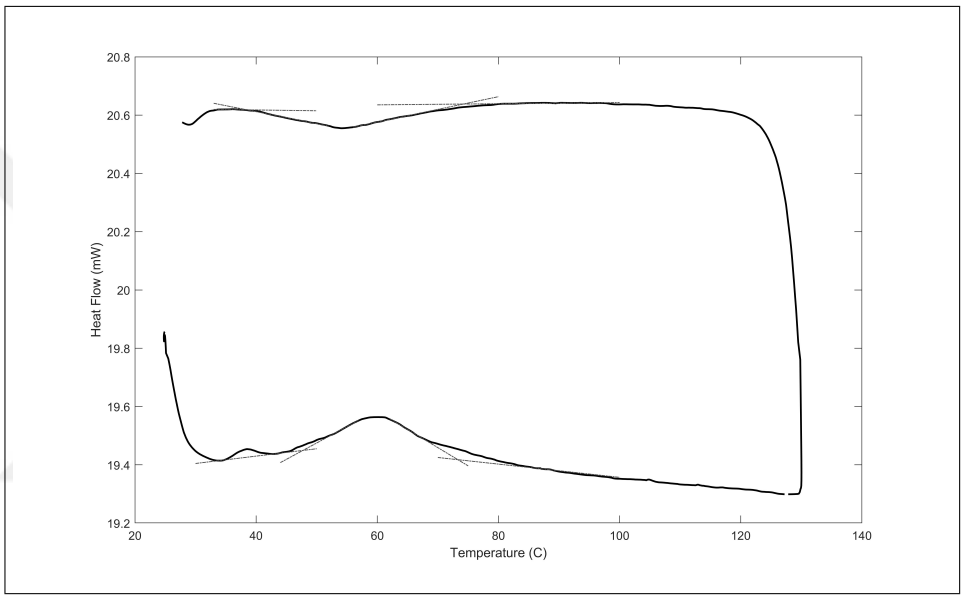

Figure 3.1 DSC graph for heating and cooling of the nitinol wire.

Figure 3.2 shows the fabricated actuator while squeezing a silicone tube. The final dimensions that were used for the actuator characterization in this study was 10mm and 20mm. Figure 3.3 shows the actuator from the side at rest and actuated states. The dimensions of the design were chosen in a way so that it can squeeze a silicone tube with 1 mm diameter.

Table 3.1
Transformation temperatures for 0.1mm wires.

M_s	M_f	A_s	A_f
73	38.5	47.5	73.5

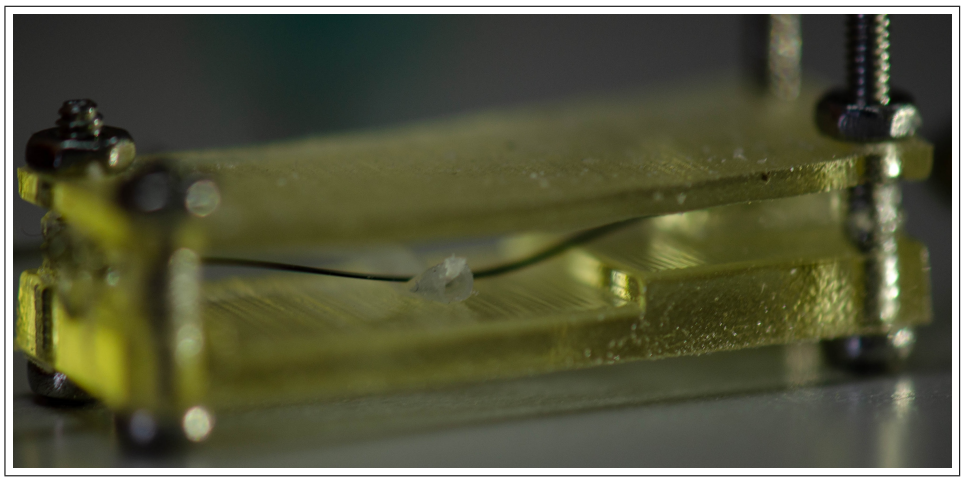

Figure 3.2 Final form of the actuator during the actuation and squeezing a silicone tube.

The buckling behavior of the flat nitinol wire was modelled using COMSOL Multiphysics software. Figure 3.4 shows a comparison between the bending profile that was predicted by the FEM before the fabrication and the actual image of the actuator after fabrication of the device. The bending profile and sideways deformation length matches that of the actual actuator.

In order to validate our choice of pseudoelastic SMAs as the buckling beam, we used a FEM model of a steel beam. Figure 3.5 shows the simulation results for the buckling of an AISI 4340 steel under the same conditions. The maximum stress in the beam under buckling reached values of 4GPa while its yield strength is 470MPa [34].

We used a hydrostatic method to measure maximum fluid pressure in channel that can be stopped by the actuator. A fluid reservoir filled with water was used to feed the fluid into the channel. Tube coming from the reservoir was connected to the actuator through a syringe. The fluid pressure in the syringe was measure using an analog manometer (Figure 3.6). The outlet of the actuator left open without any elevation. Actuator successfully closed the channel with fluid pressures of up to 150 mmHg (20KPa).

The initial tests of the actuator showed that the high temperatures of the SMA

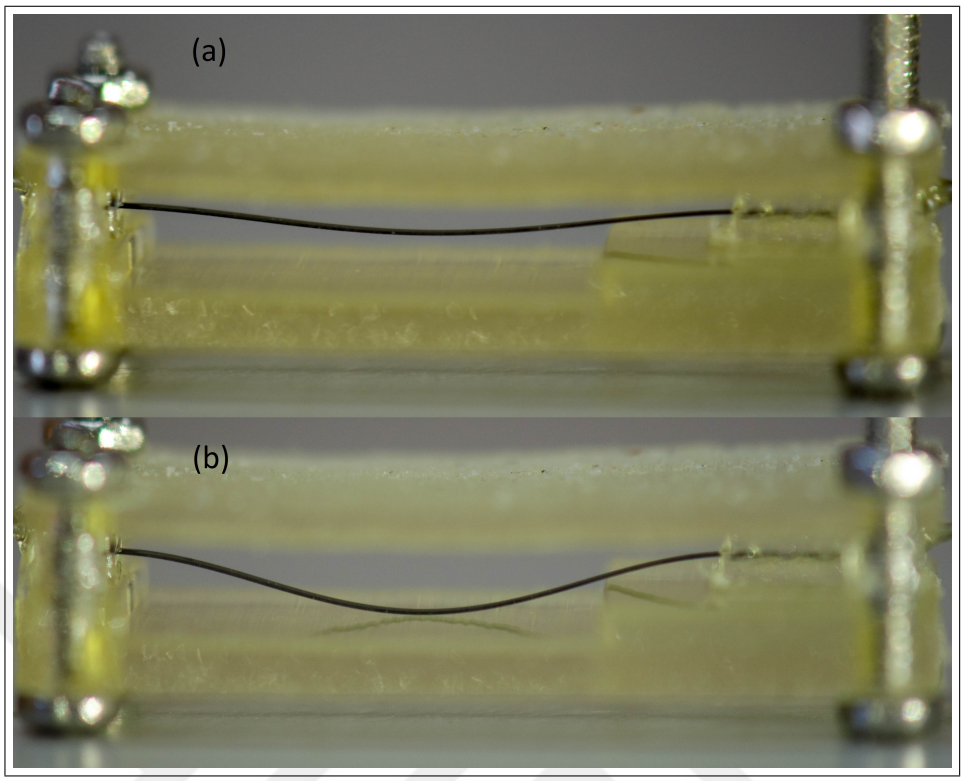

Figure 3.3 Actuator at resting(a) and active(b) states.

actuation damage the UV adhesive or the conductive epoxy adhesive. This led to loosening of the Flexinol wires. Thus, a mechanical method was implemented in order to hold the wires at the two ends of the actuator. Once the actuators were fabricated in the 3D printer, the two ends of the Flexinol wires were crimped close to the blocks and fixed using UV adhesives. This also made it easier to form the electrical connections. Since nitinol soldering is a challenging, the metal crimps at the two ends can be used as the electrical connections.

The current and voltage levels were tested to characterize the actuator. In order not to damage the actuators, the search for the ideal loading conditions started with the lower voltage and current values. The impedance measurements were done in a room temperature at 100KHz with 2V AC using Gwinstek LCR meter. Two electrode method was used. A 10%W/V NaCl solution was used for the measurements.

In the first step of the experiments no pulse width modulation was used for current control. We used a DC voltage for different actuation time periods. No pres-

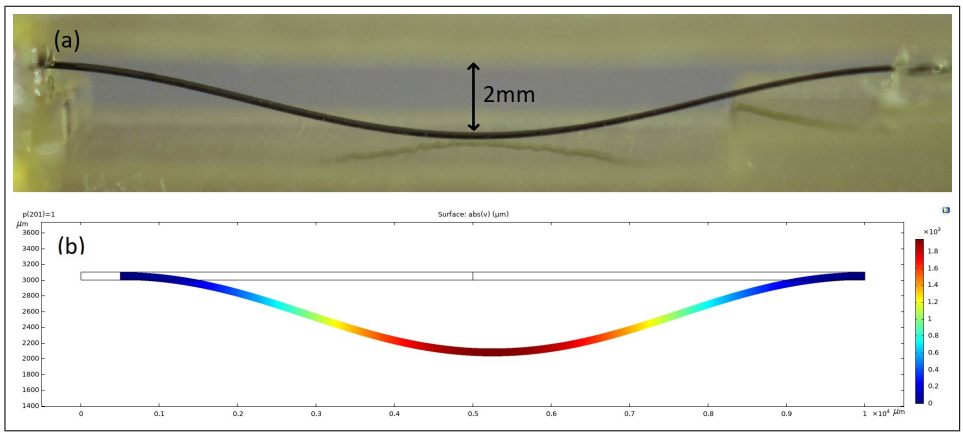

Figure 3.4 The comparison between the actual and modelled buckling behavior.

sure elevation was used during the actuation tests. Figure 3.7 shows the impedance measurements without the activation of the actuator with and without the electrolyte solution. The average impedance value for the tube with electrolyte solution inside was 1.7 $K\Omega$ while it was around 9.5 $M\Omega$ without an electrolyte solution. The measured impedance values generally oscillate a little even when the system is left intact, however, these fluctuations are completely negligible compared to the values of interests in our experiments. A control study was done by measuring the solution impedance without any perturbations in the system. The maximum oscillation in the impedance values in 1 min was shown to be less than 6 Ω which is 0.29% of the average channel impedance.

Figure 3.8 shows the slight change in impedance for 1s of actuation at 6V. It must be noted that the voltages that we report for the experiments are the voltage limit set by the power supply. However, the actual voltage that is applied to the two ends of the actuator is different due to the voltage drop across the circuit. Figure 3.9 shows the measured voltage that was applied to the actuator and current passed through when the voltage was set to 6 on power supply. As it is seen in the Figure 3.8, with the start of the actuation a 1.2 V voltage drop happens. Here we use the voltage set on the power supply for naming of the different cases, however, the net voltage and the average current passed through the actuator during different tests are summarized in Table 3.2 .

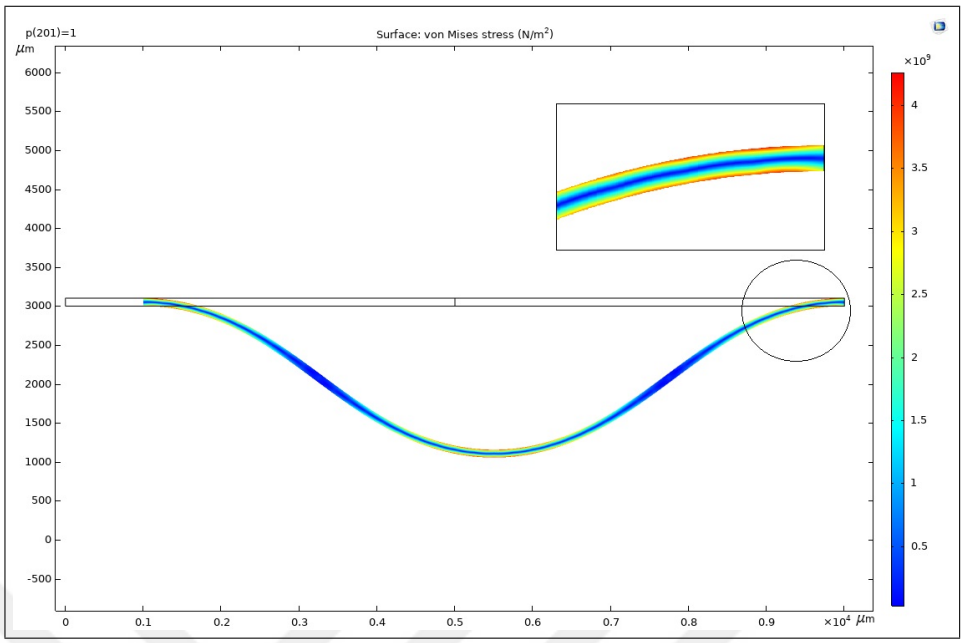

Figure 3.5 Buckling of the AISI 4340 Steel.

As it is indicated in Table 3.2, the actuator was tested in different voltages at various loading time periods. The impedance at the end of the electrical stimulation period was taken as the actuation amplitude indicator. Figure 3.10 and 3.11 show the actuation amplitudes at different voltages with various actuation times. No current limit was set by the power supply, thus the voltage was increased gradually in experiments in order not to damage the actuator. Since no significant actuation was seen at voltages lower than 7V, actuator was triggered for periods of up to 5s. However, as the voltage increased, the heating rate increases as well, which if left uncontrolled can damage the actuator. Additionally, since significant actuation was observed in stimulation times lower than 1s, for voltages greater and equal to 7V, actuation times were not longer than 1 second.

Figure 3.12 shows the impedance profile of the conductive fluid filled channel for different actuation times with 8.5V applied to the system. As it can be seen in the figure, as the stimulation period is increases, the recovery time increases as well. While no actuation can be seen in the first case (0.1s), stimulation for 0.2s, 0.3s, 0.4s, and 0.5s completely blocked the channel. Measuring the full recovery time, shows that it takes the actuator 0.45s, 0.8s, 0.9s, and 0.95s to recover after 0.2s, 0.3s, 0.4s, and 0.5s

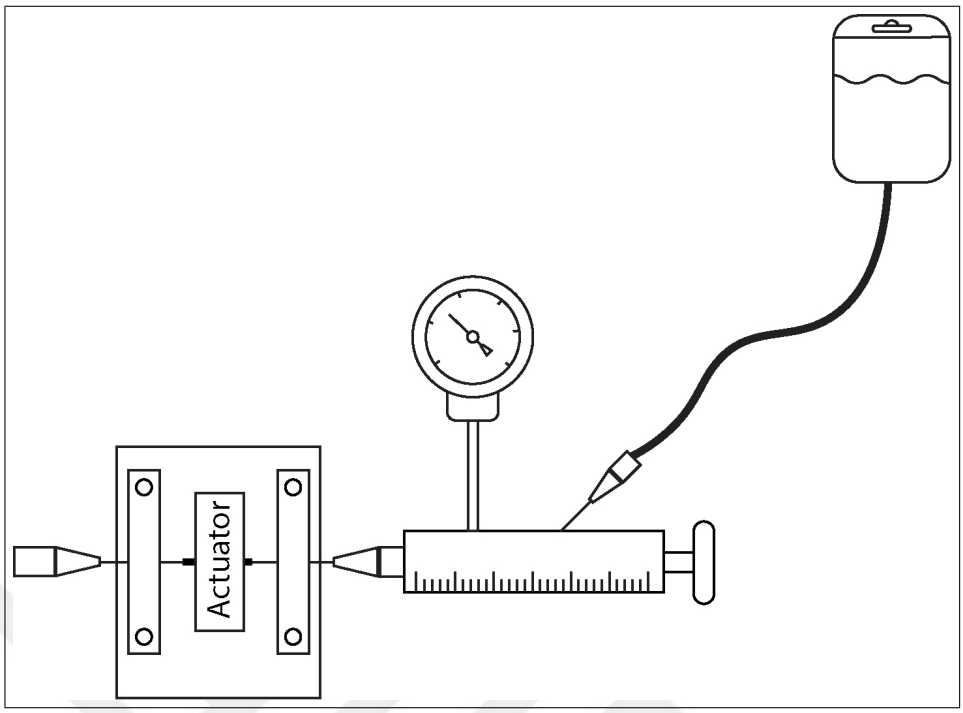

Figure 3.6 Schematic of the pressure measurement setup.

of actuation.

It must be noted that the impedance profile in almost all of the actuation tests with significant displacement shows a characteristic profile with 2 impedance overshoots at the beginning and end of the actuation. Figure 3.13 shows the impedance measurement for 0.7s of actuation with 7V. Although full blockage of the channel causes an impedance of around 100 $M\Omega$, the impedance can rise up to 120 and 170 $M\Omega$ at the first and second overshoots, respectively.

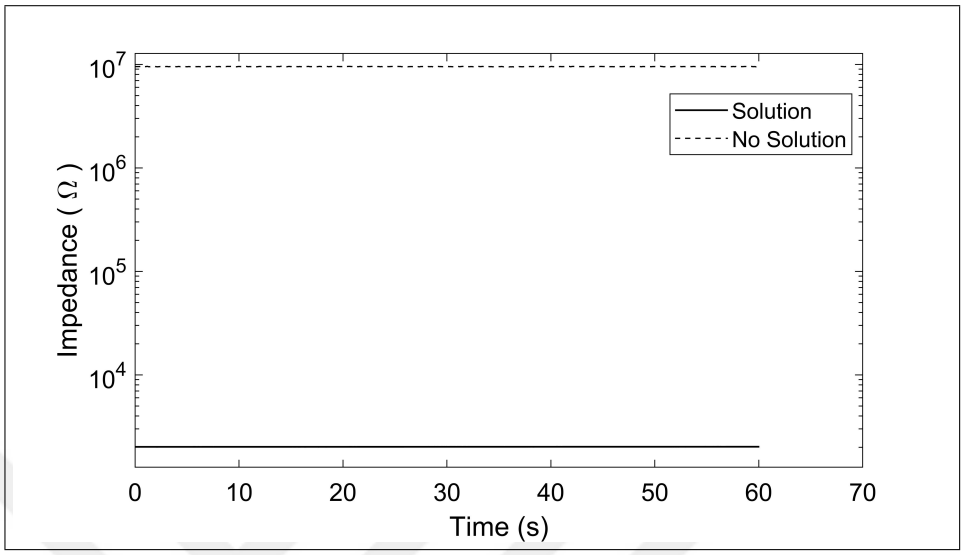

Figure 3.7 Impedance Measurement with and without electrolyte.

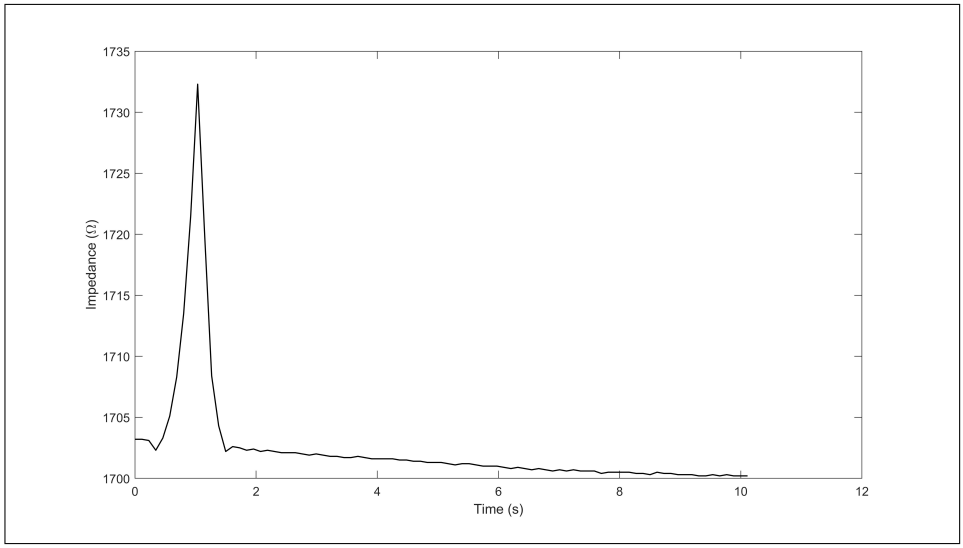

Figure 3.8 Channel impedance profile with 6V and 1s actuation time.

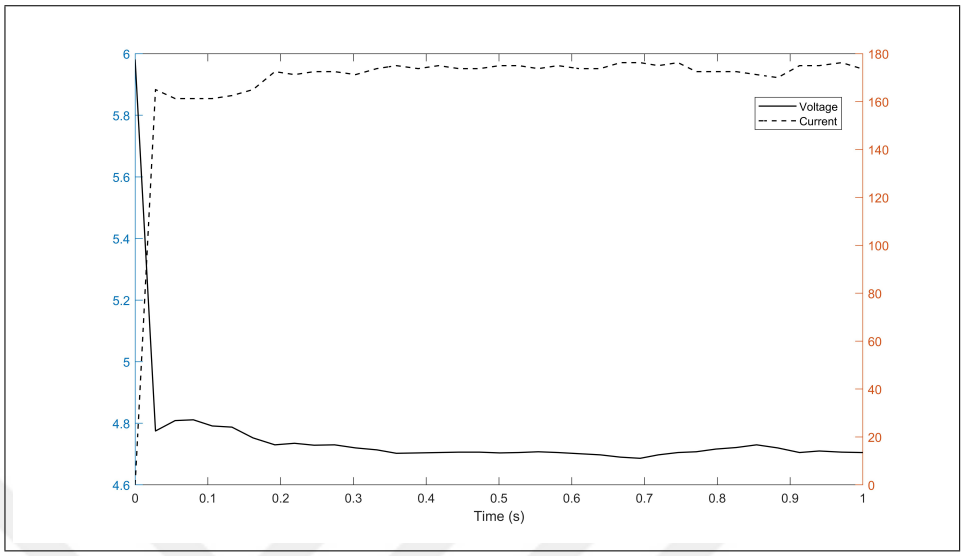

Figure 3.9 The net voltage and current applied to the SMA with 6V set on the power supply.

Table 3.2
Net voltage applied to the actuator and corresponding average current passed through the actuator during the test.

PS Voltage (V)	Net Voltage applied (V)	Mean Current (mA)
3	2.5	69.98
4	3.3	97.91
5	4.2	119.93
6	4.7	172.5
7	5.4	228.23
7.5	5.9	259.16
8	6.1	330.62
8.5	6.5	351.56
9	6.9	396.71
9.5	7.0	504.26

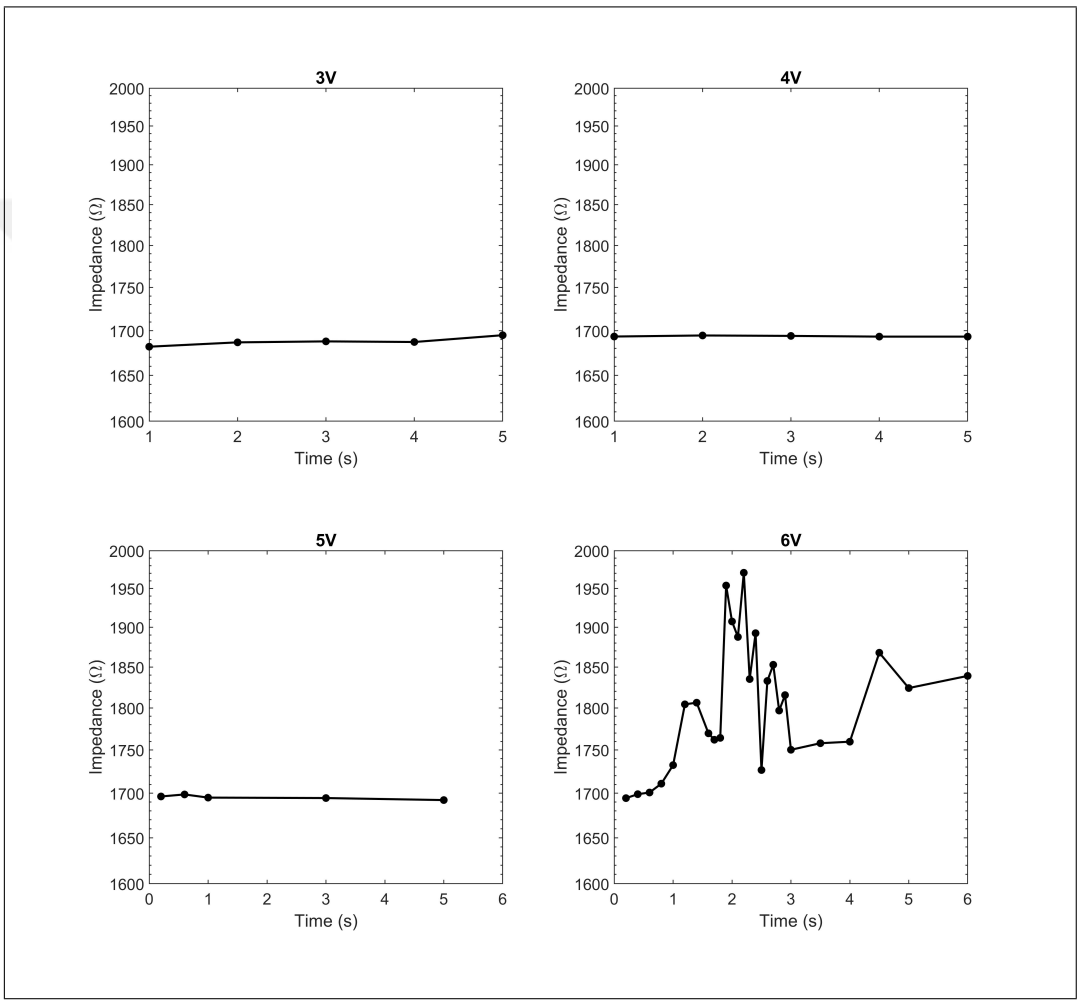

Figure 3.10 Actuation amplitude (Impedance measured at the end of the actuation time) for 3, 4, 5, and 6V with various actuation time periods.

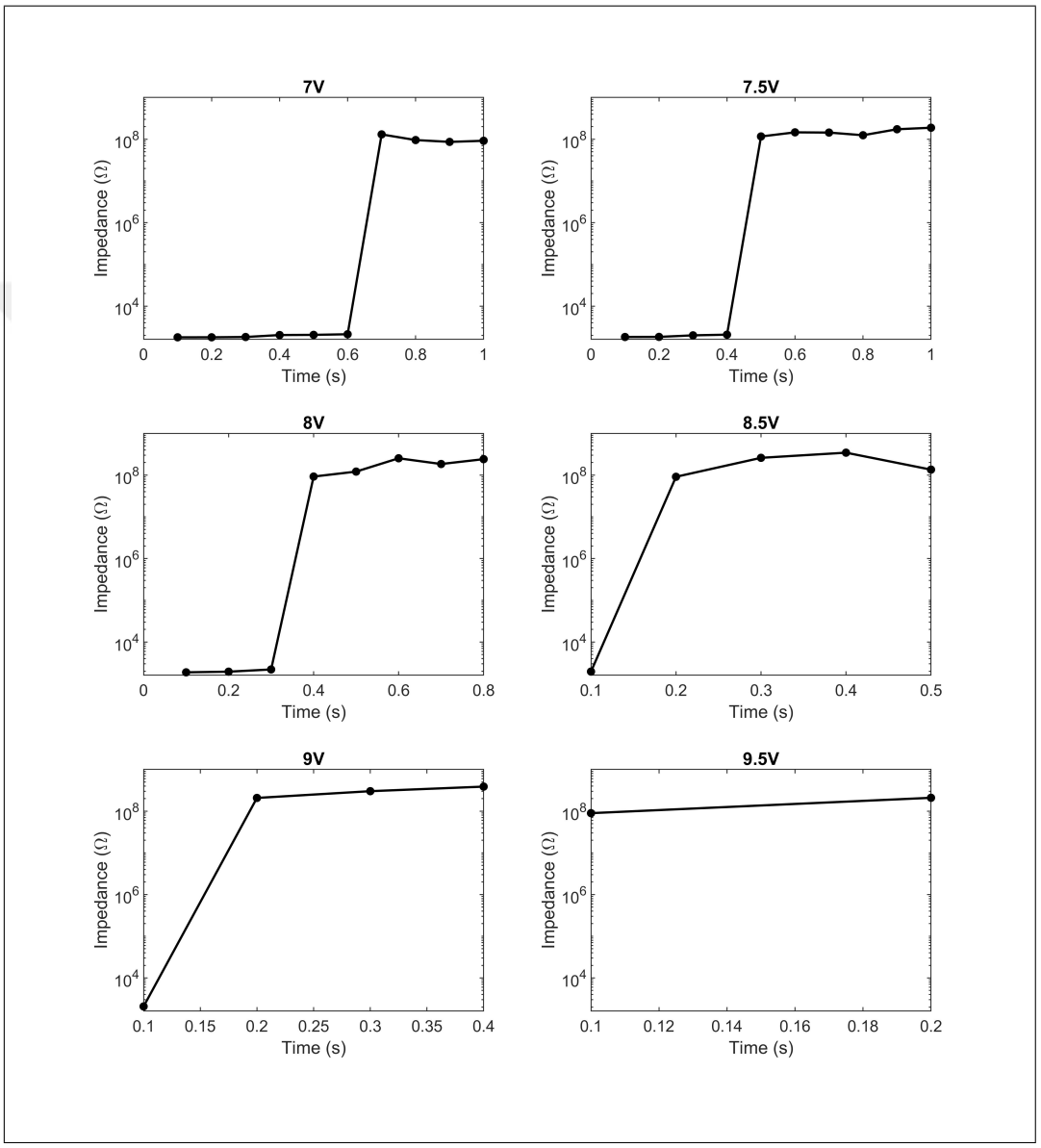

Figure 3.11 Actuation amplitude (Impedance measured at the end of the actuation time) for 7, 7.5, 8, 8.5, 9 and 9.5V with various actuation time periods.

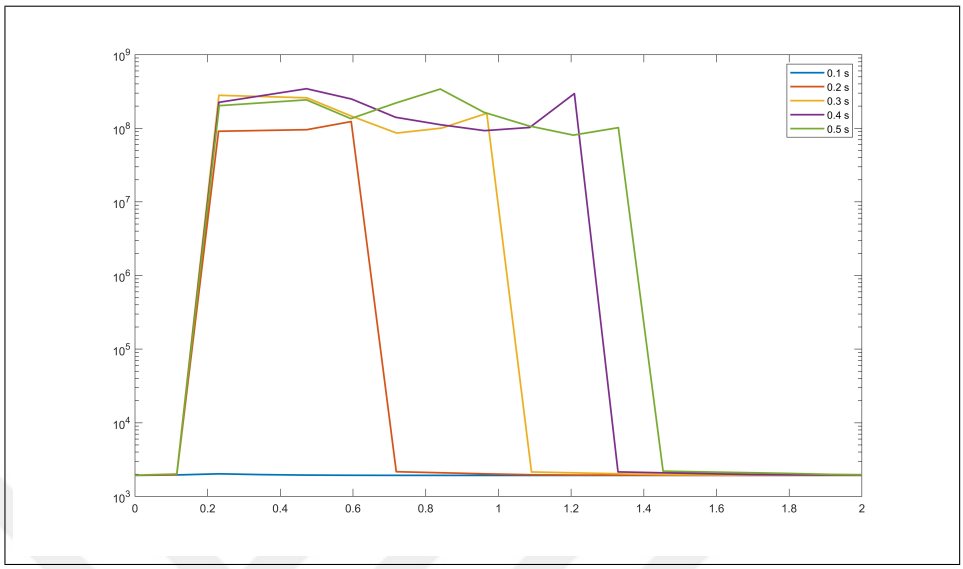

Figure 3.12 Channel impedance profile at different actuation times and 8.5V.

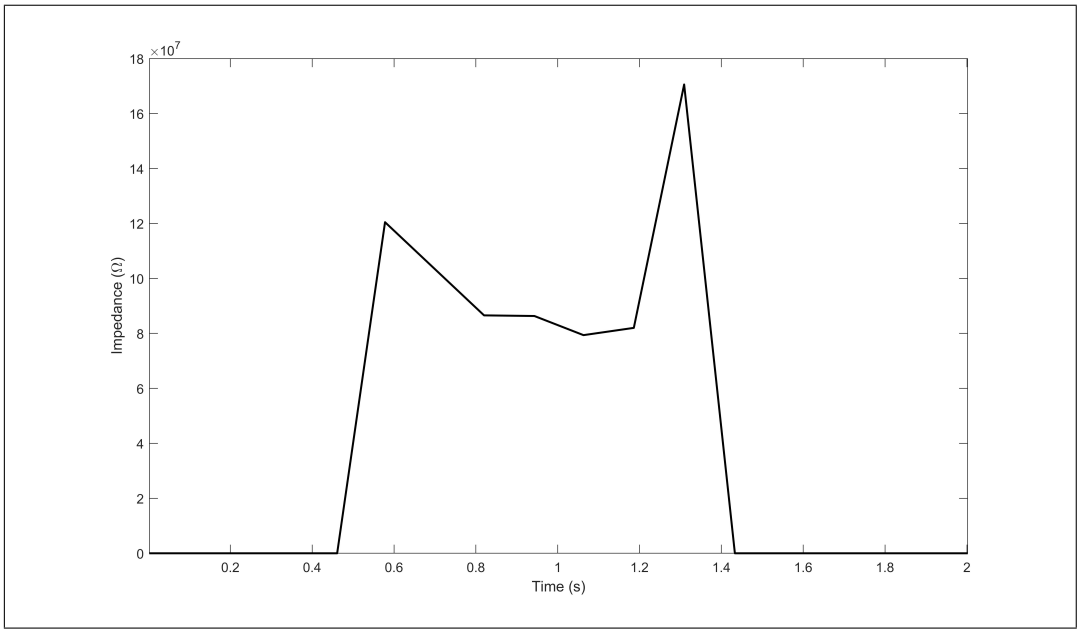

Figure 3.13 Channel impedance profile for 0.9s actuation with 7V.

4. DISCUSSION

Fabrication of the actuator was preceded by a FEM modelling of a buckling beam. Figure 3.4 shows the bending profile of a 20 mm long beam compared to the prototype actuator under similar conditions. Since the buckling profile can be calculated mathematically, we used the results from FEM as a rough guideline for selecting the dimensions of the actuator prototype. Although the bending profiles from the prototype and the model match, a complete characterization of the material is required before indulging in further quantitative analysis of the models.

Additionally, a FEM model was used to predict the approximate stresses for the buckling of a steel beam. Figure 3.5 shows the simulation results for the buckling of a steel beam with the same dimensions of the SMA beam used in our design. As it is indicated in the figure, the maximum von mises stresses in the steel beam exceeds its yield strength. This would produce high plastic strains under the same conditions in a steel beam, the recovery of which would not be possible after the first cycle of actuation.

The slight bending was seen in all of the beams in resting state (Figure 3.3). This is due to the elastic energy that was stored in the SMA wires during the fabrication. The SMA wires were loaded with 72 MPa during the fabrication process and then fixed in place. This load produces the pre-strain which we exploit for the actuation purposes. However, this strain consists of an elastic part. Once the printing support material under the loose block is removed, the elastic energy stored in the wire is partly recovered by deforming the beam. This is beneficial for the actuator's power consumption as it reduces the activation energy and reduces the response time of the actuator.

The low temperature SMA wires (A_f= 70 °C) (Dynalloy Inc.) were used in the fabrication process. Although, data-sheet is provided by the manufacturer, SMAs

tend to show batch to batch differences in their properties, thus a DSC test was used to characterize the wires in use [8]. As it is shown in Figure 3.1 and summarized in Table 3.1, the A_f and M_s temperatures are 73.5 °C and 73 °C. This indicates that the temperature hysteresis in the Flexinol wires is very low, which is favorable for high frequency actuator designs. The cycling behavior and frequency of an actuator is dependent on both the initial response time to the stimulation and it recovery time. The SMA shape recovery depends on the load applied during the cooling (i.e. bias load) and the cooling rate. The load in this design is approximately constant. Cooling of the SMA is highly dependent on the slower conductive and convective heat transfer. Small difference between A_f and M_s decreases the required heat transfer; and consequently the required shape recovery time.

The first part of every actuation cycle is the heating of the SMA. The heating rate of the SMA wire is proportional to power given by electrical stimulation which is a product of the current and voltage. In order to control the response rate of the actuator, different voltages were tested. As it is indicated in Figure 3.10, there is no actuation in voltages lower than 6V in our actuator. Taking into account that the channels impedance is around 1.700 Ω at fully open state, while it is around 6 $M\Omega$ when there is no fluid inside, it is safe to deduce that the slight perturbation which can be seen in actuation with 6V are insignificant for channel obstruction. Additionally, the visual observations during the experiments support these outcomes. However, some activity can be observed in 6V. That being said, it must be noted that, the partial actuation can be implemented in robotic systems such as stent navigation systems or controlled force applications.

Testing the actuator at voltages higher than 6 volts (Figure 3.11) showed that as the voltage increases the heating rate increases as well. As it is seen in the figure, the first significant obstruction of the fluid channel happens with 7V after 0.7s actuation. It can be seen that in each group of tests with different voltages that the channel impedance reaches a plateau after a specific loading time. This indicates that once the conductive fluid filled channel impedance reaches this plateau the channel is fully obstructed and any further stimulation of the actuator can cause overheating of the

actuator and lead to slower recovery and ultimately for higher values, failure. This is also supported by the actuation profiles shown in Figure 3.12. As it can be seen in the figure, the channel is fully closed in 0.2s, 0.3s, 0.4, and 0.5s of actuation, however, the recovery time of the the actuator increases from 450ms in the first case to 800, 900, and 950ms in the second, the third case, and forth cases respectively. This shows an approximately two fold increase in the recovery time which directly affects the cycling frequency of the actuator.

It is also indicated that this first response decreases as the voltage increases. Henceforth, for a faster response rate for high frequency applications, a high voltage with lower actuation time can be used. We increased the voltage and decreased the triggering time until we find the 100ms actuation time. It was shown that once we increase the voltage up to 9.5V (net voltage applied to the actuator 7.02V) the device is fully actuated in less than 100ms. This shows that in order to obtain a higher response rate which can be appealing for the higher frequency pumping applications, a greater voltage can be applied to the device. The inability of accurately exploring the actuation times smaller than 100ms can be explained by the limitations of the control circuit. The LabVIEW and Arduino LINX interface has a communication limit which lowers the accuracy of opening and closing of the logic gate. Thus, in the future studies a new control mechanism can be used to surpass the limits here and explore the actuators behavior in actuation times lower than 100ms with higher control accuracy.

It was very interesting to note that in all the test, as the beam starts to recover its shape, the impedance values overshoots initially and then decreases. Figure 3.13 shows the channel's impedance for the actuation test with 7V for 0.9s where this characteristic behavior is also observable. This is due to the nature of the solution conductivity. The solution conductivity is influenced by mass transfer phenomena. Once the beam starts to recover its shape and reopen the channel, the negative pressure produced in the vicinity, causes a flow in the channel. This phenomenon causes a temporary increase in the impedance before it starts to decrease. As it is seen the figure, once the actuator is activated, the impedance overshoots initially, and then reduces to a stable value. The impedance stays in such stable state provided, the actuation continues for

sufficient time. Finally, once actuator cools down enough to go to the recovery phase, the actuator overshoots once more. This characteristic overshoot of the impedance values is related to the induced flow in the channel. Ayliffe et al [35] showed that in a microchannel filled with a saline solution, the impedance significantly increases with the flow rate. In this design when the channel is deformed during the actuation, because of the small induced flow in the channel, impedance increases and once the actuator starts to recover the initial shape a second flow is produced due to the negative pressure. This produced flow can be used for the design of a micropump if used in harmony with additional actuators.

Despite the limitation of pressure tolerance experiment, we successfully showed that this design is capable of withstanding fluid pressures of up to 150 mmHg and completely obstruct the channel. This can be of high value in the design of new Chip to World interfaces for smaller microfluidic chips that use the quake valves.

5. CONCLUSION

In this study we aimed to show a proof of concept meso-scale actuator for the microfluidic applications. A set of SMA wire and pseudoelastic SMA flat wire was used in combination. We have successfully showed the ability of the actuator to produce off-plane high force actuation.

Utilizing bulk NiTi which can be obtained easily through commercial vendors, 3D printing processes, and on-board microcontrollers significantly reduced the costs of the actuator fabrication and operation compared to the available commercial units. This demonstrates the potential of this design to be used in research labs.

The proposed unique actuator design inhibits the unwanted heat transfer to the working fluid in the channel. This is very advantageous for the microfluidic applications, specially the biological applications, where the working fluid can be highly sensitive to the heat.

The novel fabrication method which is a multistep 3D printing process enables the mass fabrication of the actuator with a minimum effort. Additionally, the method that has been introduced here can be used in the design and development of actuators in other fields, such as soft robotics.

In order to characterize actuators behavior and testing the feasibility of utilizing such design in a micropump development we used a fluidic setup to characterize the device. Correspondingly, a soft custom made silicone tube with an inner diameter of 0.8mm and outer diameter of 1mm was used in the device. The tube was filled with the saline solution and the channel impedance was used as an indicator of the actuation amplitude and response rate of the actuator.

It has been shown that the response time of the actuator can be controlled by

changing the stimulation voltage and time. These actuation parameter's can be chosen based on the application with various response time requirements from values under 100ms to 6 seconds. Additionally, we have shown actuator's ability to partially close the channel which is of significance since it renders this design beneficial for other applications such as the development of world to chip interface devices.

Finally, we have tested the force that was produced by the actuator with a high pressure flow. The actuator's ability to close a channel with fluid pressures of up to 150mmHg could be tested in laboratory setup. Further studies need to be done in order to investigate the actuator's limits.

For the future studies, we are exploring two objectives:

- Implementation of such design in a meso-scale peristaltic micropump development
- Fabrication of micro-actuators with the buckling mechanism. Such actuators can be used as on chip microvalves with high force production.

REFERENCES

1. Iverson, B. D., and S. V. Garimella, "Recent advances in microscale pumping technologies: a review and evaluation," *Microfluidics and Nanofluidics*, Vol. 5, pp. 145–174, aug 2008.

2. Sosa-Hernández, J. E., A. M. Villalba-Rodríguez, K. D. Romero-Castillo, M. A. Aguilar-Aguila-Isaías, I. E. García-Reyes, A. Hernández-Antonio, I. Ahmed, A. Sharma, R. Parra-Saldívar, and H. M. N. Iqbal, "Organs-on-a-Chip Module: A Review from the Development and Applications Perspective," *Micromachines*, Vol. 9, p. 536, oct 2018.

3. D'Eramo, L., B. Chollet, M. Leman, E. Martwong, M. Li, H. Geisler, J. Dupire, M. Kerdraon, C. Vergne, F. Monti, Y. Tran, and P. Tabeling, "Microfluidic actuators based on temperature-responsive hydrogels," *Microsystems & Nanoengineering*, Vol. 4, p. 17069, jan 2018.

4. Laser, D. J., and J. G. Santiago, "A review of micropumps," *Journal of Micromechanics and Microengineering*, Vol. 14, pp. R35–R64, jun 2004.

5. Wang, Y.-N., and L.-M. Fu, "Micropumps and biomedical applications â A review," *Microelectronic Engineering*, Vol. 195, pp. 121–138, aug 2018.

6. Au, A. K., H. Lai, B. R. Utela, and A. Folch, "Microvalves and Micropumps for BioMEMS," *Micromachines*, Vol. 2, pp. 179–220, may 2011.

7. Neumann, C., A. Voigt, L. Pires, and B. Rapp, "Design and characterization of a platform for thermal actuation of up to 588 microfluidic valves," *Microfluidics and nanofluidics*, Vol. 14, no. 1-2, pp. 177–186, 2013.

8. Lagoudas, D. C., "Introduction to Shape Memory Alloys," in *Shape Memory Alloys Modeling and Engineering Applications*, ch. 1, pp. 1–51, 2008.

9. Song, S. H., J. Y. Lee, H. Rodrigue, I. S. Choi, Y. J. Kang, and S. H. Ahn, "35 Hz shape memory alloy actuator with bending-twisting mode," *Scientific Reports*, Vol. 6, no. January, pp. 1–13, 2016.

10. Yun, S., K. Lee, H. Kim, and H. So, "Development of the pneumatic valve with bimorph type PZT actuator," *Materials Chemistry and Physics*, Vol. 97, no. 1, pp. 1–4, 2006.

11. Wood, R. J., E. Steltz, and R. S. Fearing, "Optimal energy density piezoelectric bending actuators," *Sensors and Actuators, A: Physical*, Vol. 119, no. 2, pp. 476–488, 2005.

12. GmbH, P. C., "PL1XT0001 - PL112-PL140 rectangular PICMA bender piezo actuators. Technical note.," 2014.

13. Piezo systems, I., "High performance piezoelectric bending actuators.," 2010.

14. Oh, K. W., and C. H. Ahn, "A review of microvalves," *Journal of Micromechanics and Microengineering*, Vol. 16, pp. R13–R39, may 2006.

15. Lagoudas, D. C., "Thermomechanical Characterization of Shape Memory Alloy Materials," in *Shape Memory Alloys Modeling and Engineering Applications*, ch. 2, pp. 53–119, 2008.

16. Huang, X., K. Kumar, M. K. Jawed, A. Mohammadi Nasab, Z. Ye, W. Shan, and C. Majidi, "Highly Dynamic Shape Memory Alloy Actuator for Fast Moving Soft Robots," *Advanced Materials Technologies*, Vol. 4, p. 1800540, apr 2019.

17. Corporation, M., "Introduction to Nitinol," *Memry Corporation*, 2017.

18. Kapoor, D., "Nitinol for Medical Applications: A Brief Introduction to the Properties and Processing of Nickel Titanium Shape Memory Alloys and their Use in Stents," *Johnson Matthey Technology Review*, Vol. 61, no. 1, pp. 66–76, 2017.

19. Huang, S., M. Leary, T. Ataalla, K. Probst, and A. Subic, "Optimisation of NiâTi shape memory alloy response time by transient heat transfer analysis," *Materials & Design*, Vol. 35, pp. 655–663, mar 2012.

20. Ma, C., R. Wang, Q. Sun, Y. Zohar, and M. Wong, "Frequency response of TiNi shape memory alloy thin film micro-actuators," in *Proceedings IEEE Thirteenth Annual International Conference on Micro Electro Mechanical Systems (Cat. No.00CH36308)*, pp. 370–374, IEEE, 2000.

21. Leary, M., F. Schiavone, and A. Subic, "Lagging for control of shape memory alloy actuator response time," *Materials & Design*, Vol. 31, pp. 2124–2128, apr 2010.

22. Williams, E., and M. H. Elahinia, "An Automotive SMA Mirror Actuator: Modeling, Design, and Experimental Evaluation," *Journal of Intelligent Material Systems and Structures*, Vol. 19, pp. 1425–1434, dec 2008.

23. Dynalloy, "Technical Characteristics of Flexinol Actuator Wires," 2019.

24. Sofla, A., D. Elzey, and H. Wadley, "Two-way Antagonistic Shape Actuation Based on the One-way Shape Memory Effect," *Journal of Intelligent Material Systems and Structures*, Vol. 19, pp. 1017–1027, sep 2008.

25. Ishida, A., and M. Sato, "TiâNiâCu shape-memory alloy thin film formed on polyimide substrate," *Thin Solid Films*, Vol. 516, pp. 7836–7839, sep 2008.

26. Sandstrom, N., S. Braun, G. Stemme, and W. van der Wijngaart, "Full wafer integration of shape memory alloy microactuators using adhesive bonding," in *TRANSDUCERS 2009 - 2009 International Solid-State Sensors, Actuators and Microsystems Conference*, pp. 845–848, IEEE, jun 2009.

27. Clausi, D., H. Gradin, S. Braun, J. Peirs, G. Stemme, D. Reynaerts, and W. van der Wijngaart, "Design and Wafer-Level Fabrication of SMA Wire Microactuators on Silicon," *Journal of Microelectromechanical Systems*, Vol. 19, pp. 982–991, aug 2010.

28. Clausi, D., H. Gradin, S. Braun, J. Peirs, G. Stemme, D. Reynaerts, and W. Van Der Wijngaart, "Design and wafer-level fabrication of SMA wire microactuators on silicon," *Journal of Microelectromechanical Systems*, Vol. 19, no. 4, pp. 982–991, 2010.

29. Clausi, D., H. Gradin, S. Braun, J. Peirs, D. Reynaerts, G. Stemme, and W. van der Wijngaart, "Wafer-level mechanical and electrical integration of SMA wires to silicon MEMS using electroplating," in *2011 IEEE 24th International Conference on Micro Electro Mechanical Systems*, pp. 1281–1284, IEEE, jan 2011.

30. Fischer, A. C., H. Gradin, S. Schröder, S. Braun, G. Stemme, W. Van Der Wijngaart, and F. Niklaus, "Wire-bonder-assisted integration of non-bondable SMA wires into MEMS substrates," *Journal of Micromechanics and Microengineering*, Vol. 22, no. 5, 2012.

31. Clausi, D., H. Gradin, S. Braun, J. Peirs, G. Stemme, D. Reynaerts, and W. van der Wijngaart, "Robust actuation of silicon MEMS using SMA wires integrated at wafer-level by nickel electroplating," *Sensors and Actuators A: Physical*, Vol. 189, pp. 108–116, jan 2013.

32. Instruments, T., "INA260 Datasheet," 2019.

33. Orazem, M. E., and B. Tribollet, "Electrochemistry," in *Electrochemical Impedance Spectroscopy*, ch. 5, pp. 73–96, 2008.

34. AZoM, "AISI 4340 Alloy Steel (UNS G43400)."

35. Ayliffe, H. E., and R. Rabbitt, "An electric impedance based microelectromechanical system flow sensor for ionic solutions," *Measurement science and Technology*, Vol. 14, no. 8, p. 1321, 2003.